Pontifícia Universidade Católica do Rio Grande do Sul
FACULDADE DE ENGENHARIA
PROGRAMA DE PÓS-GRADUAÇÃO EM ENGENHARIA E TECNOLOGIA DE MATERIAIS

# SIMULAÇÃO COMPUTACIONAL POR DINÂMICA MOLECULAR DE FILMES FINOS ORGÂNICOS IRRADIADOS POR ÍONS PESADOS: COMPARAÇÃO ENTRE O POTENCIAL FENE E LENNARD-JONES

**NATHAN WILLIG LIMA**
BACHAREL EM FÍSICA

**DISSERTAÇÃO PARA A OBTENÇÃO DO TÍTULO DE MESTRE EM ENGENHARIA E TECNOLOGIA DE MATERIAIS**

**Porto Alegre**
**Agosto, 2016**

Pontifícia Universidade Católica do Rio Grande do Sul
FACULDADE DE ENGENHARIA
PROGRAMA DE PÓS-GRADUAÇÃO EM ENGENHARIA E TECNOLOGIA DE MATERIAIS

# SIMULAÇÃO COMPUTACIONAL POR DINÂMICA MOLECULAR DE FILMES FINOS ORGÂNICOS IRRADIADOS POR ÍONS PESADOS: COMPARAÇÃO ENTRE O POTENCIAL FENE E LENNARD-JONES

**NATHAN WILLIG LIMA**
BACHAREL EM FÍSICA

ORIENTADOR: PROF. DR. RICARDO MEURER PAPALEO

Dissertação de Mestrado realizada no Programa de Pós-Graduação em Engenharia e Tecnologia de Materiais (PGETEMA) da Pontifícia Universidade Católica do Rio Grande do Sul, como parte dos requisitos para a obtenção do título de Mestre em Engenharia e Tecnologia de Materiais.

**Porto Alegre**
**Agosto, 2016**

Pontifícia Universidade Católica do Rio Grande do Sul
FACULDADE DE ENGENHARIA
PROGRAMA DE PÓS-GRADUAÇÃO EM ENGENHARIA E TECNOLOGIA DE MATERIAIS

# SIMULAÇÃO COMPUTACIONAL POR DINÂMICA MOLECULAR DE FILMES FINOS ORGÂNICOS IRRADIADOS POR ÍONS PESADOS: COMPARAÇÃO ENTRE O POTENCIAL FENE E LENNARD-JONES

**CANDIDATO: NATHAN WILLIG LIMA**

Esta Dissertação de Mestrado foi julgada para obtenção do título de MESTRE EM ENGENHARIA E TECNOLOGIA DE MATERIAIS e aprovada em sua forma final pelo Programa de Pós-Graduação em Engenharia e Tecnologia de Materiais da Pontifícia Universidade Católica do Rio Grande do Sul.

**DR. RICARDO MEURER PAPALÉO - ORIENTADOR**

**BANCA EXAMINADORA**

**DR. PAULO FERNANDO PAPALÉO FICHTNER - ESCOLA DE ENGENHARIA - UFRGS**

Adriano Moehlecke

**DR. ADRIANO MOEHLECKE - DO PGETEMA - FENG - PUCRS**

PUCRS
Campus Central
Av. Ipiranga, 6681 - Prédio 30 - Sala 103 - CEP: 90619-900
Telefone: (51) 3353.4059 - Fax: (51) 3320.3625
E-mail: engenharia.pg.materiais@pucrs.br
www.pucrs.br/feng

# SUMÁRIO

# LISTA DE FIGURAS

# RESUMO

LIMA, Nathan. **Simulação Computacional por Dinâmica Molecular de Filmes Finos Orgânicos Irradiados por Íons Pesados: Comparação entre o Potencial FENE e Lennard-Jones.** Porto Alegre. 2016. Dissertação. Programa de Pós-Graduação em Engenharia e Tecnologia de Materiais, PONTIFÍCIA UNIVERSIDADE CATÓLICA DO RIO GRANDE DO SUL.

Nesse trabalho foram realizadas simulações computacionais por dinâmica molecular de filmes finos orgânicos irradiados por íons pesados e rápidos. Para representar a deposição de energia pelo íon foi utilizado o Modelo de *Thermal Spike*, através do qual a trilha iônica é representada como uma região cilíndrica de alta temperatura ao longo do material. Dois artigos foram submetidos para publicação a partir desse estudo. No primeiro artigo, o impacto da espessura do filme e da energia do íon incidente nos efeitos topológicos da radiação (como diâmetro da cratera, profundidade da cratera e volume da protuberância) e do sputtering foram investigados, comparando-se os resultados de sólidos cristalinos e amorfos modelados pelo potencial de Lennard-Jones. No segundo artigo, o potencial FENE foi implementado para construir amostras com cadeias moleculares. Os efeitos da radiação iônica foram então comparados entre os filmes com cadeias moleculares (modelados pelo potencial FENE) e filmes sem cadeias moleculares (modelados com o potencial de Lennard-Jones). Em ambos os trabalhos, os efeitos da radiação foram explicados verificando-se os diferentes mecanismos de dissipação de energia: evaporação, *melt flow* e deformação plástica. Nossos resultados mostram que os efeitos da radiação são fortemente impactados pela espessura do filme. As simulações com o potencial FENE mostram que a presença de cadeias moleculares reduz significativamente todos os efeitos da radiação. Para sólidos mais finos que o raio de giração médio das moléculas, nenhum efeito da radiação foi observado, indicando que a redução dos efeitos está relacionada não só à diminuição de mobilidade, mas também à conformação e emaranhamento molecular.

Palavras-Chaves: irradiação de íons pesados, filmes finos, dinâmica molecular.

# ABSTRACT

LIMA, Nathan. **Molecular Dynamics Simulation of organic thin films irradiated by heavy ions: a comparison between Lennard-Jones and FENE potentials.** Porto Alegre. 2016 . Master Thesis. Graduation Program in Materials Engineering and Technology, PONTIFICAL CATHOLIC UNIVERSITY OF RIO GRANDE DO SUL.

In this work, molecular dynamics simulations of thin organic films irradiated by fast heavy ions were implemented. In order to represent the ion energy deposition, it was used a Thermal Spike Model, in which the ion track is represented as a cylindrical region with high temperature. Two papers were submitted for publication based on this study. In the first paper, it was studied the impact of film thickness and the ion energy in the topological effects of radiation (such as crater diameter, crater depth and rim volume) and in the sputtering, comparing the results for a crystalline and amorphous solids modeled by the Lennard-Jones potential. In the second paper, the FENE potential was implemented to build samples with molecular chains. The ionic radiation effects were then compared between films with molecular chains (modeled by the FENE potential) and without molecular chains (using the Lennard-Jones potential). In both works, the effects of radiation were explained by analyzing the different mechanisms of energy dissipation: evaporation, melt flow and plastic deformation. Our results show that radiation effects are strongly determined by film thickness. The simulations with FENE potential show that the presence of molecular chains reduces significantly the effects of radiation. In solids thinner than the mean gyration radius of the sample, there was not any radiation effect, indicating that the effect reduction is related not only to the decreasing of mobility but also to molecular conformation and entanglement.

Key-words: heavy ion irradiation, thin films, molecular dynamics.

# 1. INTRODUÇÃO

O uso de íons pesados para estudar as propriedades da matéria remonta ao trabalho pioneiro de Ernest Rutherford, cujos resultados trouxeram uma nova visão sobre a estrutura atômica e revolucionaram a Física no início do século XX. Nas décadas subsequentes, a radiação iônica passou a ser utilizada em diferentes aplicações tecnológicas, tanto com o objetivo de caracterizar bem como de modificar materiais de forma controlada.

Na Medicina, por exemplo, a terapia por prótons [1] ou íons pesados [2] utilizam íons para danificar células cancerígenas em regiões de alta radiossensibilidade. Mais recentemente, novas técnicas de imageamento como radiografia [3] e tomografia [4] por prótons vem sendo utilizadas para otimizar os tratamentos protonterápicos. A microeletrônica é outro exemplo de grande relevância tecnológica em que os íons podem ser utilizados (para realizar dopagem de semicondutores) [5]. Nas geociências e em ciências de materiais, outros problemas também podem ser encontrados em que a radiação iônica se apresenta como uma alternativa para a modificação e caracterização controlada de materiais, incluindo datação de materiais antigos, estabilização e reticulação de plásticos, entre outros.

O uso de íons para caracterizar materiais tem também ganhado relevância, principalmente, no estudo de materiais orgânicos e biológicos (em que predominam macromoléculas fracamente ligadas) [6]. A Espectrometria de Massas por Íons Secundários (*Secondary Ion Mass Spectrosmetry* – SIMS) utiliza íons para ejetar macromoléculas de uma amostra, que são posteriormente identificadas por um espectrômetro de massa [7]. O SIMS é limitado, entretanto, pelo baixo rendimento de íons secundários de moléculas de alta massa - principalmente na faixa de energia em que foi inicialmente utilizado (na ordem de kiloetronvolt) [8]. A partir da década de setenta, novas técnicas foram implementadas, utilizando íons pesados rápidos (com energia na faixa de megaeletronvolt) como PDMS, e, mais recentemente, MeV-SIMS

[7]. Existe um grande interesse no MeV-SIMS, pois ele apresenta maior rendimento (*sputtering yeld*) e menor taxa de fragmentação quando comparado com o SIMS tradicional. Esse incremento de rendimento ainda não é completamente bem entendido [8]. Por isso, existe um esforço dentro da comunidade internacional para avançar no estudo de *sputtering* causado por íons de alta energia. Além disso, foi demonstrado que feixes de íons primários com MeV podem ser usados para gerar mapas de concentração molecular na superfície, considerado o primeiro uso do MeV-SIMS [9]-[11].

Mais recentemente, com os avanços na nanociência e na nanotecnologia, íons pesados rápidos vêm sendo empregados para modificar materiais de forma altamente controlada em escala nanométrica, uma vez que a trilha de excitação formada pela radiação tem um raio de poucos nanômetros [12]. Os nanomateriais irradiados são, então, utilizados para a criação de materias nanoporosos, que podem ser usados como moldes para a produção de nanofios ou como parte de sistemas de *drug delivery*, desenvolvimento de máscaras para formação de nanotubos de carbono entre outros [13], [14].

Os efeitos da radiação, da mesma forma que outras propriedades de um material, são alteradas quando esse é confinado na escala nanométrica - muitas vezes por um motivo inerentemente geométrico [15]. Dessa forma, garantir que aplicações da radiação em materiais em nanoescala sejam implementadas de forma controlada e com alta precisão é necessário se entender como que o confinamento espacial impacta os efeitos da radiação. Os resultados experimentais podem fornecer informações sobre o estado inicial e final do sistema irradiado, mas não são capazes de prover detalhes sobre a evolução dos efeitos da radiação (que acontecem na escala de centenas de picosegundos) [16]. Para avançar no estudo da evolução dos sistemas, modelos teóricos e simulações computacionais são indispensáveis [17].

Nesse trabalho, efeitos induzidos pela radiação iônica na superfície de filmes ultrafinos são estudados usando simulação computacional por dinâmica molecular. Essas simulações consistem na solução das equações de Newton para cada partícula do sistema a cada intervalo de tempo pré-determinado [17]. A cada interação, as posições, os momentos e as forças atuando sobre cada partícula são calculados servindo como dado de entrada para os cálculos do passo subsequente. Assim, é possível acompanhar a evolução de cada partícula bem como sua velocidade e sua energia a cada passo da evolução do sistema e, posteriormente, as propriedades termodinâmicas do sistema podem ser computadas recorrendo-se a conceitos de Mecânica Estatística [18].

Esse trabalho tem por objetivo principal estudar os efeitos da radiação iônica em filmes ultrafinos orgânicos utilizando simulação por dinâmica molecular. O primeiro objetivo específico é estudar as diferenças dos efeitos da radiação em filmes ultrafinos cristalinos e amorfos para diferentes energias de íon incidente e espessuras dos filmes. O segundo objetivo é incluir explicitamente a presença de cadeias moleculares nas amostras irradiadas, comparando a evolução do sistema, o sputtering e a formação de nanoestruturas na superfície com resultados obtidos nas simulações em filmes amorfos sem cadeia molecular.  Os dados dos simulação nos dois casos foram comparados com experimentos obtidos em filmes finos de polímeros.

Para atingir os objetivos propostos, as simulações por dinâmica molecular foram implementadas no Laboratório de Alto Desempenho da PUCRS [19] utilizando a ferramenta computacional LAMMPS [20]. Para simular a perturbação no sistema introduzida pelo íon,  utilizou-se um modelo conhecido como *Thermal Spike* [21], [22] que considera a evolução do sistema a partir do momento em que a rede eletrônica já transferiu a energia para a rede atômica, e a energia depositada pode ser representada como uma região cilíndrica de alta temperatura no interior do material. Optou-se por implementar simulações na escala granular (em que cada monômero é descrito como uma partícula), pois simulações em escala verdadeiramente atomística implicariam um aumento elevado de custo computacional. Para descrever o material cristalino e amorfo, foi utilizado o potencial de Lennard-Jones [23], e para descrever o material com cadeia molecular foi utilizado o potencial FENE [24]. Para os dois estudos, filmes de 2nm a 60nm foram simulados para estudar o impacto do confinamento espacial nos efeitos da radiação.

No capítulo 2.2 é apresentada uma breve fundamentação desse trabalho em que se discutem conceitos importantes de interação da radiação iônica de alta energia com a matéria e conceitos importantes de simulação computacional por dinâmica molecular. No capítulo 2.3 são apresentados dois artigos: *Simulations of cratering and sputtering from an ion track in crystalline and amorphous Lennard Jones thin films* e

*Molecular dynamics simulation of polymer-like thin films irradiated by fast ions: a comparison between FENE and Lennard-Jones potentials.* O primeiro artigo (submetido no periódico *Physical Review E*), do qual sou co-autor, apresenta uma comparação entre efeitos da radiação em sólidos amorfos e cristalinos e compreende os resultados obtidos na dissertação de mestrado de Leandro Gutierres e resultados obtidos por mim ao longo do mestrado. O segundo artigo (submetido ao periódico *Physical Review B*), do qual sou autor principal corresponde ao assunto central dessa dissertação. Nele são apresentadas as comparações dos efeitos das radiações em sólidos com cadeias moleculares e sem cadeias moleculares, que foram obtidos por mim com colaboração do Prof. Dr. Eduardo Bringa da Universidade de Cuyo e do Dr. Rafael Gonzalez da Universidade do Chile.

# 2. FUNDAMENTAÇÃO TEÓRICA

Nesse capítulo é apresentada uma breve fundamentação teórica dos artigos originais desse trabalho. Na primeira seção, são definidas as grandezas essenciais para o estudo da interação da radiação iônica com a matéria, apresentados os principais efeitos da radiação e os últimos resultados obtidos sobre o impacto do confinamento espacial nos efeitos da radiação, os quais foram utilizados diretamente na análise de resultados dos dois artigos. Na segunda seção, é apresentada uma breve explicação sobre o funcionamento de Simulações Computacionais por Dinâmica Molecular.

## 2.1. Interação de Radiação Iônica com a matéria

Ao interagir com a matéria, íons podem transferir energia para os núcleos dos átomos do meio ou para a rede eletrônica. Essa interação pode ser mensurada através da grandeza chamada *stopping power* (S) – definida como a quantidade de energia (dE) depositada pelo íon por unidade de comprimento (dx) [25], [26] – que pode ser subdividida em *stopping power* nuclear ($S_n$) ou eletrônico ($S_e$) de acordo com o alvo da deposição de energia:

$$S = \frac{dE}{dx} = S_e + S_n \tag{1}$$

Pela figura 2.1 [27], percebe-se que íons rápidos possuem *stopping power* eletrônico muito superior ao *stopping power* nuclear (para um próton de 100 MeV em PMMA, por exemplo, $S_e/S_n$ = 2.591), de tal forma que é possível afirmar que o íon interage predominantemente com a rede eletrônica do material. Essa característica é muito importante, pois, transferindo energia para os elétrons, o íon tem seu momentum praticamente inalterado, fazendo com que sua trajetória seja, em média, retilínea ao longo do material. Além disso, o íon rápido desencadeia cascatas eletrônicas, que resultam, por fim, na modificação do material em uma zona muito estreita (com raio na ordem de poucos nanômetros) [12].

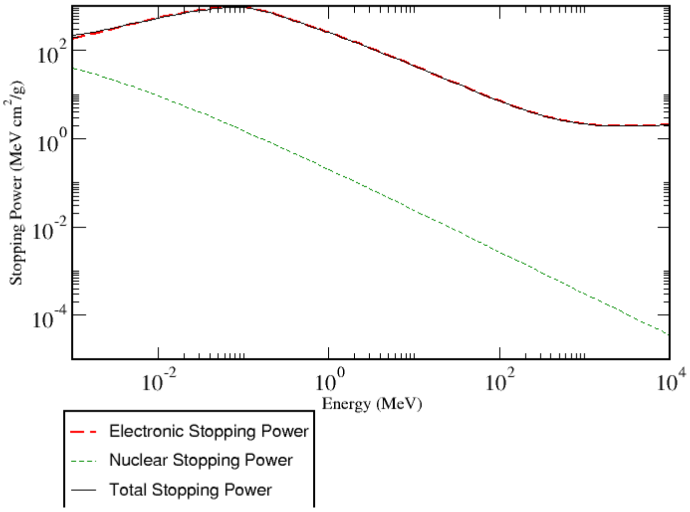

Figura 2.1. Gráfico de *stopping power* eletrônico, nuclear e total em função da energia para prótons em PMMA [27]. Pode-se perceber que, com o aumento da energia do íon incidente, existe uma queda no *stopping power* nuclear indicando que o íon interage predominantemente com a rede eletrônica). O *stopping power* está em unidades de MeVcm²/g de forma que deve ser multiplicado pela densidade do PMMA para se obter o *stopping power* total.

É claro que, se o material for espesso (*bulk*), a perda de energia do íon dentro do material faz com que exista uma mudança de regime de freamento, e o íon passa a interagir com os núcleos atômicos e a ser defletido. No caso de filmes ultrafinos, isso não acontece e é possível afirmar que o íon penetra o material criando uma região de dano com simetria cilíndrica em torno de sua trajetória. O caminho percorrido pelo íon, bem como o caminho percorrido pelas partículas secundárias resultantes da interação formam o que é chamado de *ion track*, ou rastro do íon.

O *track* pode ainda ser subdivido em *infratrack* (região em que ocorrem as ionizações primárias) cujo diâmetro é de 1-4 nm e o *ultratrack* (região em que acontecem os danos causados pelos elétrons secundários) cujo diâmetro pode chegar a 40 nm para íons com 0,6 MeV/u [28]. Em materiais isolantes, o *track* é formado por uma distribuição de partículas excitadas e ionizadas, espalhadas radialmente ao redor da trajetória do íon. Apenas uma fração da energia depositada (de 10%-40%) [29],

[30] pelo íon na rede eletrônica é transferida para rede atômica na forma de energia cinética. Esse aumento médio de energia cinética por partícula (<k>) pode ser interpretado como um aumento de temperatura (T), usando a relação:

$$< k > = \frac{3}{2} k_b T \tag{2}$$

Onde $k_b$ é a constante de Bolztmann. Com os valores de *stopping power* conhecidos, pode-se estimar que a temperatura inicial do *infratrack* assume valores tão altos quanto dezenas de milhares de kelvins. A partir dessa ideia, surgiu na década de oitenta, o Modelo de *Thermal Spike [21]*. Inicialmente proposto de forma analítica, o Modelo de *Thermal Spike* resolve a equação do calor, considerando o *infratrack* como um cilindro de alta temperatura no interior do material. A figura 2.2 mostra uma imagem de simulação computacional, em que o *infratrack* aparece como uma região cilíndrica de T = 25.000 K em um filme orgânico de 60 nm de espessura.

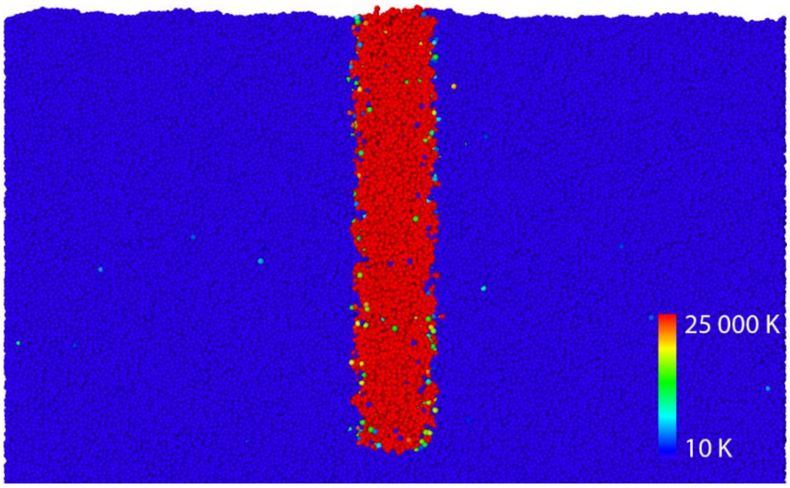

Figura 2.2. Imagem de simulação computacional implementada com modelo de *Thermal Spike*. Vê-se um corte no meio do material, onde o *infratrack* aparece como uma região cilíndrica de 25000 K. A espessura do filme é 60 nm. Abaixo do filme, existe a representação do substrato (fonte: o autor).

Além da formação do *track*, o íon rápido é capaz de formar efeitos topológicos no material como cratera e protuberância [31]-[33], além de ejetar moléculas e fragmentos de moléculas (*sputering) [34], [35]*. A figura 2.3 mostra uma imagem de AFM em que pode se identificar a formação de crateras e protuberâncias causadas por um íon de Pb com 923 MeV em PMMA com incidência normal à superfície [36]. A dimensão lateral do filme apresentado na figura 2.3.a é de 250 nm. Três crateras (regiões escuras) com profundidade de aproximadamente 2,5 nm podem ser identificadas na figura 2.3.a. Ao redor da cratera, existe a formação de uma protuberância (regiões claras) com altura de aproximadamente 2,5 nm. Na figura 2.3.b, parte da imagem é ampliada e pode-se perceber que a protuberância não assume uma distribuição isotrópica ao redor da cratera.

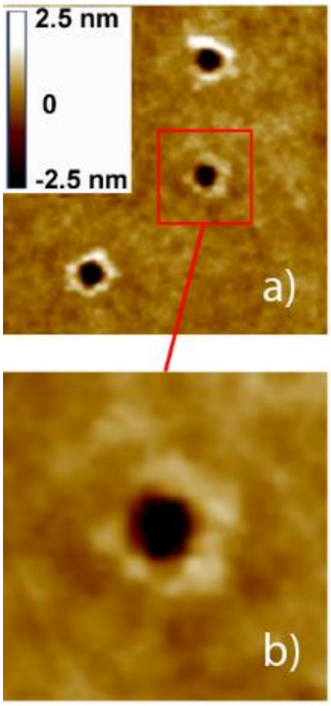

Figura 2.3. Imagem de AFM de efeitos topológicos causado por íon de Pb com 923 MeV em um filme de PMMA com 40 nm de espessura [36]. Pode-se observar a cratera como a região mais escura (representando uma profundidade de 2,5 nm) em relação a superfície. Ao redor das crateras, percebe a formação de uma protuberância, região em que o material alcança uma altura até 2,5 nm acima da superfície (adaptado da ref.36). Na figura 2.3.a, vê-se corte do filme com dimensões laterais de 250 nm com 3 crateras. Na figura 2.3.b, vê-se uma cratera ampliada.

Nosso grupo publicou alguns artigos indicando a dependência dos efeitos da radiação iônica em matéria orgânica com relação a diferentes parâmetros físicos, como angulação do íon incidente [32], [37], temperatura do material irradiado [38] e estado de carga [39].

Existem ainda poucos estudos que mostrem o impacto do confinamento espacial nos efeitos da radiação de uma forma sistemática, isto é, que comparem os resultados obtidos com material *bulk* em relação a materiais confinados espacialmente. Fenyö e Johnson [40] apresentaram um trabalho pioneiro em que mostram o impacto do confinamento espacial na ejeção de moléculas em um sólido amorfo. Para isso, eles utilizaram simulação computacional por dinâmica molecular modelando o sólido amorfo com o potencial de Lennard-Jones e compararam os resultados com um modelo analítico chamado de Modelo do Pulso de Pressão.

Nesse modelo, proposto inicialmente, para o caso *bulk*, supõe-se que a energia de excitação recebida pelos átomos do *track* é convertida em movimentação das moléculas. Essa movimentação causa a expansão do material contra a região não excitada e o vácuo. Cada molécula excitada causa, portanto, uma distribuição de densidade de energia ϵ' no material. A densidade de energia total em um determinado ponto a uma distância ρ do track e em uma profundidade z do material é obtida somando-se os impulsos gerados ao longo de todo o track:

$$\epsilon(\rho, z, t) = \int_0^h \epsilon'(r, z, t) \frac{dz}{\lambda} \tag{3}$$

onde $\lambda^{-1}$ é o número de fontes por unidade de comprimento ao longo da trilha e h é a espessura do filme. O esquema geométrico do problema é mostrado na figura 2.4.

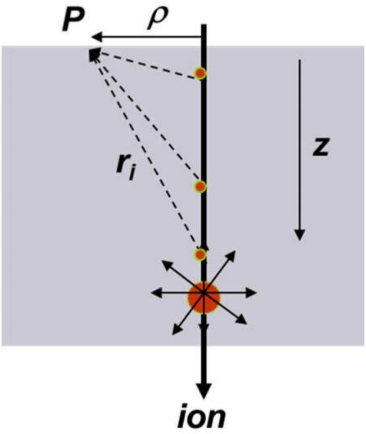

Figura 2.4. Esquema da trilha de impulsos ao longo da trajetória do íon (adaptado da ref. [41]).

A partir disso, pode-se calcular o impulso total recebido por uma molécula como:

$$\Delta p = \beta V_m \int_0^t \nabla\epsilon \, dt \tag{4}$$

Onde β é uma constante de proporcionalidade $V_m$ é o volume molecular. Se o momento Δp ultrapassa um valor crítico, pode-se dizer que a molécula é ejetada, caso contrário, ela permanece no material. A integral em (7) expressa, portanto, o caráter aditivo dos impulsos gerados, o que relaciona, portanto, os efeitos da radiação com a espessura do filme. Os resultados de Fenyö e Johnson mostram que o *sputtering* aumenta com o aumento da espessura até chegar em um certo valor crítico, para o qual o aumento da espessura não impacta mais o rendimento do *sputtering.*

Na tese de doutorado de Raquel Thomaz [41], o Modelo de Pulso de Pressão foi utilizado para avaliar o impacto do confinamento espacial nos efeitos topológicos da radiação iônica, comparando-os com dados experimentais. A figura 2.5. mostra mapas de momento linear gerados para filmes de 100nm (Fig. 2.5.a) e 10 nm (Fig. 2.5.b).

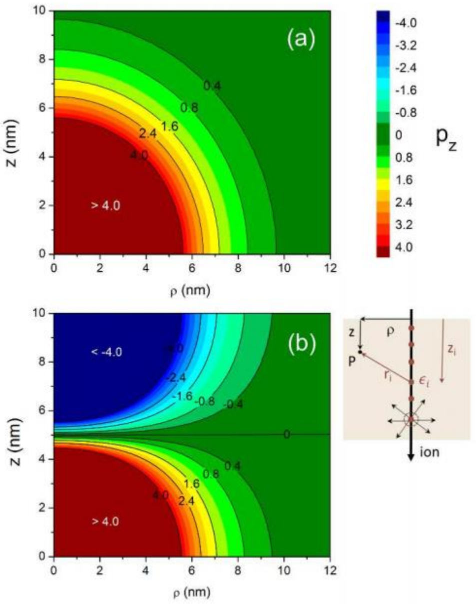

Figura 2.5. Mapas de momento para filme com 100 nm (a) e 10 nm (b). A escala de cores representa o momentum pz e as linhas nos gráficos indicam segmentos onde $p_z$ é constante. Um esquema das coordenadas do sistema é mostrado à direita dos mapas, onde a origem é ponto de penetração do íon na superfície. (Adaptado da ref. [41]).

Uma vez que a energia depositada em um certo ponto tem caráter aditivo, é possível mostrar que a função $\epsilon$ é simétrica em relação a h/2. Como o momentum depende de $\nabla\epsilon$, todas partículas acima de h/2 apresentam momento positivo e todas partículas abaixo de h/2 apresentam momento negativo, como mostrado na figura 2.5.b. No caso de filmes espessos, h/2 está muito abaixo da superfície, e todas moléculas na região de interesse apresentam momento positivo. Esse modelo coloca, portanto, um limite geométrico na profundidade da cratera igual à metade da espessura do filme. Da mesma forma, nenhuma partícula ejetada do material deve vir de uma profundidade maior do que h/2. Embora esse modelo não tenha sido usado diretamente nessa dissertação, ele foi utilizado para discutir os resultados obtidos nos dois artigos.

Com os dados obtidos a partir do modelo do Pulso de Pressão, dados experimentais e dados de simulação computacional, Papaleo et al [36] mostraram que o confinamento espacial tem um impacto significativo em efeitos topológicos da radiação (figura 2.6). Independentemente de terem sido obtidos por vias experimentais ou teóricas, esses apresentam o mesmo comportamento qualitativo: os filmes apresentam resistência à radiação para espessuras menores do que um certo valor crítico, de forma que os efeitos são muito pequenos para filmes ultrafinos. Com o aumento da espessura do filme, os efeitos também aumentam, até chegar em uma certa espessura crítica, onde o aumento da espessura não implica um aumento do efeito (região de plateau na parte direita dos gráficos chamada de região de *bulk*).

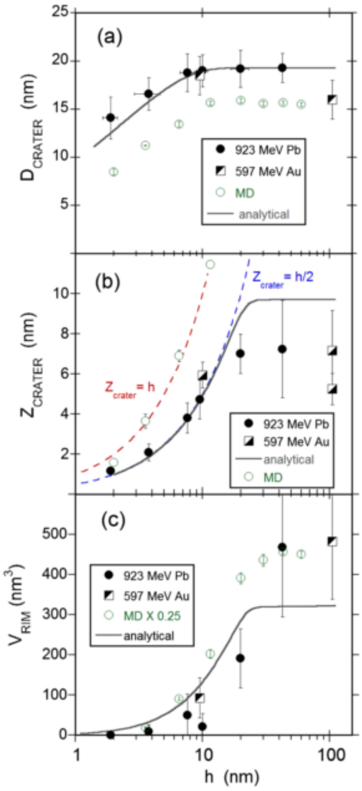

Figura 2.6. Diâmetro da cratera (2.6.a), profundidade da cratera (2.6.b) e volume da protuberância (2.6.c) em função da espessura do filme para dados experimentais de Pb com 923 MeV, Au com 597 MeV, simulação computacional por dinâmica molecular e modelo analítico do pulso de pressão. [36].

## 2.2. Simulação Computacional por Dinâmica Molecular

Simulações Computacionais são ferramentas muito importantes para mediar resultados experimentais e modelos teóricos, podendo, muitas vezes, corroborar novas teorias ou indicar a necessidade de novos experimentos [17], [18]. Dependendo da escala de grandeza em que se está estudando e do problema estudado, diferentes estilos de ferramenta computacional podem ser utilizadas, como Monte Carlo, Dinâmica Molecular Semi-Clássica, Dinâmica Molecular, Métodos Finitos, entre outros. A Simulação Computacional por Dinâmica Molecular (SCDM) é uma ferramenta desenvolvida para solucionar o problema de interação de múltiplos corpos. Esse problema, conhecido originalmente para o sistema solar, não possui solução analítica para três corpos ou mais [18].

Mesmo sabendo que o nível molecular está compreendido nos limites da Mecânica Quântica, muitas características da matéria, em nível molecular, podem ser explicadas de forma clássica. A solução numérica das equações de Newton para interações moleculares é, portanto, o objeto de estudo da SCDM e, usualmente implica na aplicação de um algoritmo de integração. O método mais simples possível é conhecido como *leapfrog*, que calcula a velocidade e a posição das partículas da seguinte forma:

$$\vec{v_i}\,(t + \Delta t/2) = \vec{v_i}\,\left(t - \frac{\Delta t}{2}\right) + \Delta t.\vec{a_i}\,(t) \tag{5}$$

$$\vec{r_i}(t + \Delta t) = \vec{r_i}(t) + \Delta t.\overrightarrow{v_i}(\;t + \frac{\Delta t}{2}) \tag{6}$$

onde $\vec{v_i}(t)$ e $\vec{a_i}\,(t)$ são a velocidade e a aceleração da i-ésima partícula do sistema no tempo t respectivamente. $\Delta t$ é chamado de *timestep,* tempo decorrido entre duas interações ( cujo valor é decisão do programador).

Para implementação da SCDM, além de um algoritmo de integração, é necessário descrever a posição e velocidade iniciais de cada partícula do sistema bem como o potencial de interação entre elas. Para calcular a aceleração de cada partícula em um tempo t, usam-se as equações de Mecânica Clássica:

$$\vec{a_i}\,(t) = \frac{\vec{F_i}(t)}{m_i} \tag{7}$$

onde $\vec{F_i}(t)$ é a força resultante atuando sobre a i-ésima partícula. Para conhecer a força resultante, deve-se ainda calcular o somatório sobre o gradiente da energia potencial causado por todas as demais partículas do sistema:

$$\vec{F_i}(t) = \sum \nabla Ui \tag{8}$$

Um potencial muito utilizado é o potencial de Lennard- Jones [23], que descreve a interação entre partículas de um sólido de gás condensado.

$$\boldsymbol{E_{LJ} = 4\epsilon[\left(\frac{\sigma}{r}\right)^{12} - \left(\frac{\sigma}{r}\right)^{6}]} \tag{9}$$

onde $\epsilon$ é uma constante de proporcionalidade com dimensão de energia, σ tem dimensão de distância e r é a distância entre duas partículas. O potencial de Lennard-Jones tem a característica de se tornar repulsivo quando partículas estão mais próximas do que o raio de equilíbrio (pela predominância do termo com potência 12), e de se tornar atrativo quando partículas estão além da distância de equilíbrio ( pela predominância do termo com potência 6). O raio de equilíbrio pode ser calculado, derivando-se a energia potencial em relação a r para obtenção da expressão da força e igualando a zero, de tal forma que $r_{eq} = \sigma\ 2^{1/6}$. Além disso, com o afastamento das partículas, a energia potencial cai rapidamente de forma que o potencial é nulo para partículas infinitamente distantes. Na prática, para aumentar a eficiência computacional, estabelece-se uma distância de corte, de tal forma que partículas mais distantes do que o valor de corte produzam uma energia potencial desprezível e não precisem ser avaliados pelo computador – o que reduz significativamente o tempo de simulação. Apesar da simplicidade do potencial de Lennard-Jones, muitos trabalhos já utilizaram esse potencial para avaliar efeitos da radiação em filmes orgânicos, obtendo-se resultados qualitativamente similares aos dados experimentais [32], [36], [37], [40], [42].

Nesse trabalho, além de se usar o potencial de Lennard-Jones, usou-se o potencial FENE [24], para modelar os polímeros na escala granular, isto é, representando cada monômero como uma partícula. A vantagem do potencial FENE é que ele permite a construção de cadeias moleculares. Dessa forma, ao se construir um sólido com o potencial FENE, faz-se a distinção entre ligações intramoleculares ( que são descritas pelo potencial FENE) e ligações intermoleculares ( descritas pelo potencial de Lennard-Jones). A expressão do potencial FENE é mostrado na equação (8):

$$\boldsymbol{E_{FENE}} = -0.5KR_0{}^2 \ln\left[1-\left(\frac{r}{R_0}\right)^2\right] + \boldsymbol{4\epsilon}\left[\left(\frac{\sigma}{r}\right)^{\boldsymbol{12}} - \left(\frac{\sigma}{r}\right)^{\boldsymbol{6}}\right] + \epsilon \quad (10)$$

O potencial FENE incorpora um termo logarítmico ao potencial de Lennard-Jones. Esse termo tende a zero quando r tende a zero, de forma que o potencial é predominado pela parte repulsiva do potencial de Lennard-Jones para pequenas distâncias. Quando r se aproxima de $R_0$, o termo logarítmico tende a infinito, criando uma barreira de potencial para partícula, que não consegue se afastar mais do que a distância $R_0$ previamente determinada. Na expressão (8), K é uma constante de proporcionalidade. Essa expressão só é válida para duas partículas dentro da mesma cadeia. Partículas pertencendo a cadeias distintas interagem apenas pelo potencial de Lennard-Jones. A figura 2.7 mostra um gráfico para expressão do potencial FENE.

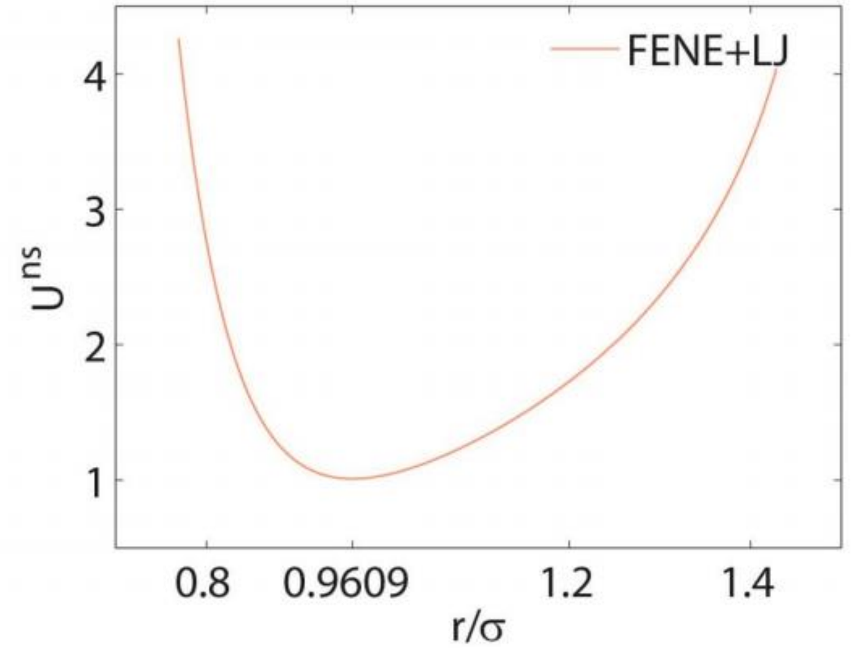

Figura 2.7. Gráfico da energia potencial gerada pelo FENE. O eixo y apresenta valores de energia em uma escala arbitrária e o eixo x expressa distância em termos de r/ $\sigma$. [43].

O fato de o potencial FENE crescer muito rapidamente conforme r se aproxima de $R_0$ cria uma complicação metodológica no uso desse potencial para modelar sólidos irradiados por íons de alta energia, pois, no início da simulação, as velocidades iniciais das partículas pertencentes ao *track* são muito elevadas. Isso pode conduzir a erros de convergência se o valor escolhido de *timestep* não for pequeno o suficiente.

Para contornar esse desafio, optou-se por utilizar um algoritmo com *timestep* variável, em que o valor do *step* fosse limitado pela movimentação das partículas. Assim, se conseguiu garantir a convergência das integrações numéricas.

# 3. PRIMEIRO ARTIGO ORIGINAL

## Simulations of cratering and sputtering from an ion track in crystalline and amorphous Lennard Jones thin films

L. I. Gutierres[1], N.W. Lima[1], R. S. Thomaz[1], R. M. Papaléo[1], and E. M. Bringa[2]

[1] Faculdade de Física, Pontifícia Universidade Católica do Rio Grande do Sul, Av. Ipiranga 6681, 90619-900 Porto Alegre, Brazil

[2]CONICET and Facultad de Ciencias Exactas y Naturales, Universidad Nacional de Cuyo, Mendoza, 5500, Argentina

### ABSTRACT

Impacts of swift heavy ions of different energy loss in amorphous and crystalline Lennard-Jones (LJ) thin films (2-60 nm) were simulated using classical molecular dynamics to study cratering and sputtering, and to compare with experimental data on polymer thin films. Crater size is determined mostly by evaporation and melt flow from the hot ion track, while rim size is determined both by melt flow and by coherent displacement of particles due to the large pressure developed in the excited region. Sputtering yields from both crystalline and amorphous samples are similar, including the scaling with energy loss, but craters and rims are much smaller in crystalline films due to faster cooling. We found a strong dependence of crater size and sputtering yields on the film thickness *h* below a critical value, which is different for crater diameter and for rim volume, because of the different mechanisms involved. For all simulated thicknesses on amorphous films, the crater depth reaches almost the entire thickness of the film, but ejected particles originate mostly ( >94%) from a depth *z* <h/2. Despite the simplicity of the LJ model, the simulations reproduce remarkably well several of the experimental features seen recently on polymer thin and ultrathin films irradiated with swift heavy ions.

**keywords**: swift heavy ions, craters, polymers, molecular dynamics

## INTRODUCTION

Swift heavy ions (SHI) penetrating solids lead to extreme levels of highly localized electronic excitations, which may produce damage tracks [1-3], electronic sputtering [4, 5], phase transitions [6], cratering [7, 8] and other topographic features [9-11]. Such effects have been widely explored to tailor materials properties in a broad spectrum of technological applications. Even if the initial excitation state was known, the subsequent non-equilibrium processes leading to lasting material modification have time scales from femtoseconds to microseconds, and are poorly understood. This problem has been treated from many different theoretical viewpoints. There are thermal spike models which focus on thermal effects [12-14], including various two temperature models [2, 15]. There are also models which focus on pressure effects alone [16], and models where modification is produced above a critical energy [17] or energy density/pressure, like the pressure pulse model [18]. The presence of a surface, together with phase transitions and transport properties, which depend on temperature and density, however makes the quantitative applicability of these models problematic, as Jakas et al. [19] showed, by solving the full set of fluid dynamics equations for this problem.

As an alternative to semi-analytical models, molecular dynamics simulations (MDS) of thermal spikes and two temperature models have proven useful to model complex effects in bulk materials, and materials with an “infinite surface”. Classical MD simulations can use heating models to include the role of electronic excitations and help explain experimental results on track radii [20-22], sputtering yields [12, 18, 23-25], and crater sizes [26, 27] in different materials, from frozen gases and inorganic solids to complex organic compounds or nanoparticles [28]. In particular, MDS of a Lennard-Jones material were able to obtain qualitative agreement with experiments of cratering in polymers, including the dependence of crater size with ion velocity and angle of incidence [27]. Recently, this model was used to fit data in a study of confinement effects of ion tracks in thin polymer films [25] in which radiation effects at the surface were shown to be size-dependent below a critical thickness.

In this work, simulations on SHI irradiation of ultrathin films from a LJ solid, described preliminary in Ref. [25] are presented in detail. We first analyze and compare crater formation and particle ejection from amorphous and crystalline samples, including temperature effects and the relevance of different mechanisms involved. In a second part, we focus on film thickness effects on cratering and sputtering, comparing MDS results to recent experiments in PMMA thin films. The strong thickness dependence observed for the crater size is explained in terms of the processes involved: melt flow, pressure-pulse, and phase change. Despite the simplicity of the LJ model, the results present very good qualitative agreement with experimental data.

## SIMULATION METHODS

Molecular dynamics simulations were carried out with LAMMPS [29] at the computer cluster of the Laboratory of High Performance (LAD), PUCRS. Although there are several ways to mimic electronic excitations in classical MD simulations [18, 21, 28], the present simulations were mostly motivated by experiments on thin polymer films, and were carried out as previously done for “bulk” polymers [27]. Polymer molecules were simply modeled assuming each monomer is a particle ($m$=1,66.10$^{-22}$g, as in a PMMA monomer) interacting via a Lennard-Jones (LJ) potential with parameters $\sigma$=0.5 nm, $\varepsilon$=0.07 eV and cut-off radius of 2.5$\sigma$. The time, in reduced LJ units, relates with the mass ($m$), $\sigma$, and $\varepsilon$, via $t_{LJ} = \sigma(m/\varepsilon)^{1/2} \sim 1.9ps$. Each 1000 calculation steps correspond to about 1.9 ps, since the timestep command was set to 0.001.

We used crystalline samples as in previous work [24, 27, 30] and also amorphous samples obtained following the methodology described in [28]. Crystalline samples have a face centered cubic (fcc) structure, with a [001] surface as in most previous studies [24]. Tracks in amorphous LJ systems have been simulated previously, but for nanoparticles [28] not films, except for the preliminary results in [25]. Simulation boxes were centered at the origin and had both top and bottom free surfaces perpendicular to the z axis. All other surfaces include a region of Langevin thermostating and damping with thickness $2\sigma$. Periodic boundary conditions were applied in xy directions. Simulated targets had about 4 million particles, which was enough to avoid significant boundary effects for the track sizes and temperatures used. In some cases, 2-5 simulations were carried out for the same irradiation condition, and the resulting standard deviation in feature sizes was always less than 15%, and smaller than experimental uncertainties.

To model the ion track produced by normal incidence, molecules within a cylinder of radius $R_{track}$= 2-8 $\sigma$ (1-4nm) centered near (x,y)=(0,0) were given an energy distribution with 3/2 kT =5-50 T* (or track temperatures in reduced units T* from 5 to 50), over a time of 0.2 $t_{LJ}$. The energy deposited along the ion path which was effectively transferred into atomic motion - the $(dE/dx)_{eff}$ - was simply assumed as the total energy input into the system by this temperature increase, divided by the length of the track. The $(dE/dx)_{eff}$ values obtained scaled linearly with T*. The relationship between this simulated dE/dx and the experimental value of the electronic energy loss $(dE/dx)_{el}$ is not straightforward, since there are several possible channels for excitation decay, which may not be related to crater formation and sputtering. We assume a simple proportionality relationship, where both are connected by an efficiency parameter, which is often taken to be around 0.2, i.e. $(dE/dx)_{eff} \sim 0.2\ (dE/dx)_{el}$ [9, 31]. Many irradiation conditions were simulated by varying the track radii and initial temperature. Therefore, a large number of scenarios have been simulated, compared to the focused simulations in ref. [25]. Our parametric study of track excitation allow us to compare results for several irradiation conditions (projectile/target combinations), but in the following, we will present mostly those cases that can be directly compared to relevant experimental data on polymer thin films.

The system was allowed to evolve during at least ~100 $t_{LJ}$, and this evolution was followed with OVITO [32]. For every simulation, this time was enough to ensure that crater features had not changed size during the last stage of the simulation. However, this does not guarantee the lack of possible extremely slow thermal relaxation processes [33], but their effect should be small, given that the final temperature of the crater area was significantly below the melting temperature of the solid.

In order to model a thin film, the particles were artificially labeled as belonging to the film or the substrate according to their initial depth within the sample, and the track was heated only within the film thickness *h*. As the total box size was the same for all simulations, 80x80x80 $nm^3$, thinner films had thicker substrates and vice-versa. Thus, in our model system there is no actual film-substrate interface, as both are made of the same material. Still, the absence of a spike in the substrate means it is treated as a material where electronic excitations are relaxed before coupling to atomic motion. This is a reasonable assumption for crystalline Si [7], a common substrate in thin film experiments. Of course at the film/substrate interface, exchange of energy implies that crater features might be influenced by the substrate. This is negligible for thick films, but not for ultrathin films (*h*<5 nm) and very hot tracks (more than 20,000 K).

## RESULTS

### a) **Particle ejection and cratering formation**

Figure 1 shows a 3D view of simulated craters for both amorphous and crystalline samples. The crater includes a large rim, as also seen in simulations of keV atomic [26] and cluster [34] ions, and larger projectiles [34, 35]. Such similarities point to general formation processes involving atoms displaced by momentum transfer, phase transitions and plasticity. In the case of cluster bombardment of a LJ system [34], solid-vapor transition and melt flow were found to contribute to crater formation, mostly due to a piston effect by the incident cluster, but here the liquid flow proceeds as a kind of “fountain effect”, as described for collision cascades [36] and ion tracks [19]. For a cubic fcc crystal dense packing occurs along <111> directions and this is the most efficient direction for energy transport. Observed from the top of a (001) surface, as in Figure 1 a, this results in 4-fold symmetry in the surface plane, and a highly plane-oriented crater rim. On the other hand, the amorphous solid does not contain any preferential orientation, thus the rim has a circular shape, in agreement with the cylindrical hot track.

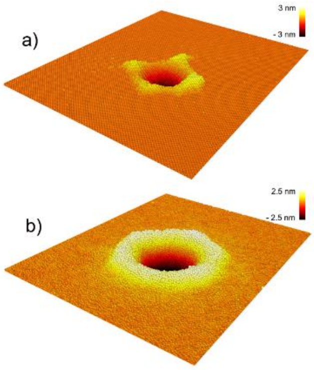

Figure 1. 3D view of crystalline (a) and amorphous (b) samples at the end of the simulation for a thickness h=10 nm, $R_{track}$=2 nm and T*=25. Coloring depicts particle height, with brighter color indicating higher regions. The cubic crystalline geometry results in the 4-fold symmetry of the crater rim in the crystalline sample, while the round rim reflects the lack of preferential directions in the amorphous sample.

Figure 2 shows kinetic energy profiles for crystalline and amorphous samples, ~10 ps after the spike for a track radius of 3 nm. Top and side views are shown of a thin slice in the center of the impact point. Closed-packed <111> directions lead to faster energy transport, and the profiles display the resulting four-fold symmetry, given that we have a (001) surface, as mentioned above for the crater rim. The amorphous sample on the other hand, shows the expected circular expanding profile. The slower energy dissipation and cooling of the excited region in the amorphous sample is evident in Figure2. The very hot central region (labeled red, with mean particle energies above the vaporization temperature) and the molten region (colors from light blue to yellow) are both longer and wider in the amorphous films. Consequently, the molten region around the ion track is sustained for a longer time in the amorphous sample, leading to larger craters and rims due to substantial melt flow, as will be later discussed. Supplemental Figure 1 shows a series of snapshots of the track evolution for 30nm thick crystalline and amorphous films, where the dynamics of energy dissipation and crater formation can be seen in detail [37].

Figure 3 exhibit a thin slice of an amorphous sample, with particles colored by their displacement with respect to their original positions, and the displacement vectors between those positions. Some isolated particles of course move to the surface due to focusons [38], but movies of the crater evolution, created using OVITO [32], shows that these groups moved coherently, due to the pressure pulse produced by the track (see for instance Supplemental Movie 1 [37]).

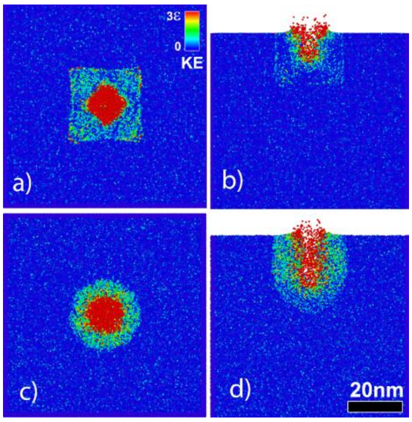

Figure 2. Kinetic energy color maps for 20 nm thick amorphous (a-b) and crystalline (c-d) films 10 ps after the spike. Left column shows top view plots, while right column shows a side view at the center of the crater. The initial track radius is 3 nm and T*=25. The energy scale is given in terms of ε.˝E. Energy is preferentially propagated along nearest neighbor <111> directions in the crystalline sample, leading to fast and efficient energy dissipation.

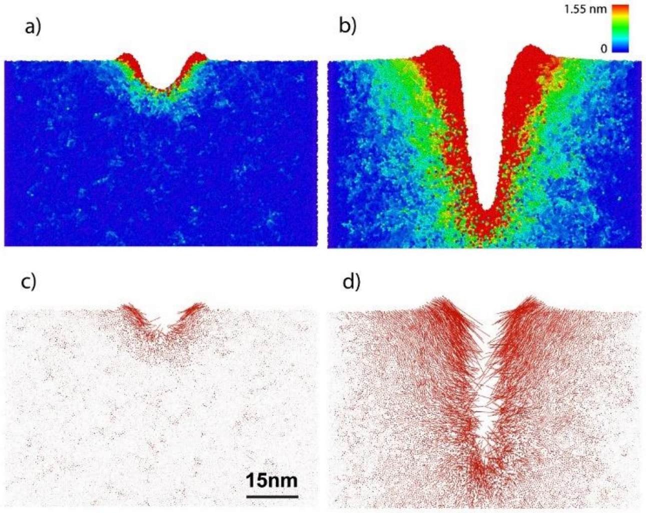

Figure 3. Final (t=190 ps) displacements and displacement vectors from original positions of particles around the ion impact site (T*=25, $R_{track}$=3 nm) for amorphous films of h=5 nm (a,c) and h=20 nm (b,d). Color is coded by displacement magnitude. Red coloring starts when displacement is bigger than 2 lattice parameters). Vectors larger than a lattice parameter indicate melting/vaporization. Most of the sputtered particles and the top rim layers originate from regions which suffered a phase transition.

Typically, the first layer of the rim is composed of thin platelets pushed out by a pressure pulse, plus some liquid flow decorating the side and top of those platelets. Such platelets are similar to the ones resulting from cooperative atomic motion due to sub-surface collision cascades [39]. This pressure effect occurs as predicted by the “pressure-pulse” model, successfully used for electronic sputtering of organic materials [40]. For thinner films, the sum of impulses leading to the pressure pulse is reduced and there is a threshold effect with thickness, as discussed later in the text.

Regarding the role of plasticity, Figure 4 compares defects remaining after cooling of the crystalline and amorphous samples. Defects have been filtered using centrosymmetry parameter. There are a few vacancies (seen by the defective atoms surrounding them), a dislocation loop at the bottom of the crater, and a few interlocked stacking faults (SF). The low stacking fault energy of the LJ solid will lead, under large stress, mostly to partial dislocations with a SF behind [41]. Most partial dislocations and SFs recover and disappear under unloading, as the crater cools down and stress decreases, and their role in the final crater volume would be minimal, unlike what occurs for craters in fcc metals by large cluster bombardment [34, 35]. Dislocation junctions might survive the cooling of the track, in this case immediately below the crater and the void which remains just below the crater, as can be clearly seen for the crystalline solid in Supplemental Figure 1. [37]. This is similar to what is observed in nanoindentation simulations of fcc solids [42]. For the amorphous sample, small clusters of particles that have re-crystallized due to heating and stress are seen in Fig. 4b (in blue). Given their small sizes, their influence in the final crater dimensions should be negligible.

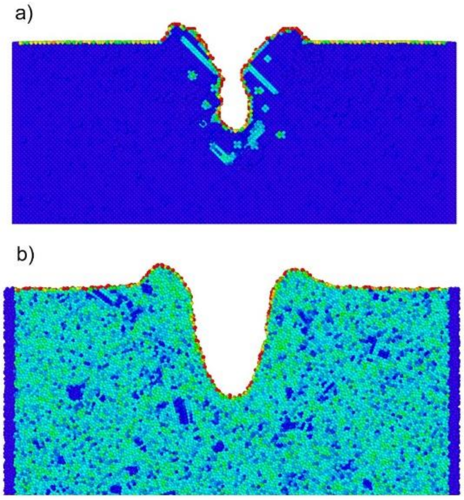

Figure 4. Final snapshot (t=190ps) of a 20 nm thick film for an ion track of T*=25 and $R_{track}$=3 nm, showing “defective” regions. The slices of (a) crystalline and (b) amorphous samples are colored by centrosymmetry from 0 (perfect crystal, blue) to 4 (red). Defects are seen in the crystalline sample (stacking faults and point defects surrounding the crater, and a dislocation loop below the crater). There are a few recrystallized regions in the amorphous sample, observed as blue clusters.

The pressure required to push a step out and contribute to the rim, or to create dislocations, could be estimated from a simple strength model. Given a hemispherical feature like the crater, the stress to deform the surrounding material plastically is roughly Gb/2R, where G is the shear modulus, R is the crater radius and b is a dislocation core size, of order 1. For a LJ crystal, G~50 [43]. In the region where there is a rim, R~10, and plasticity is ~2.5 in the early stages. Energy density leads to an initial pressure of ~12, rapidly decaying due to energy loss by an outgoing shock wave and thermal conduction away from the track. Therefore, the stress required for plasticity is easily overcome by the pressure resulting from the track, which can still reach values of 4-6 in the region surrounding the track after 19-30 ps. In the region where the rim disappears, the pressure cannot be kept for long and does not reach high values after ~19 ps. For the amorphous LJ solid, a typical threshold for plasticity is given when the shear stress reaches values of ~1.5 [44], and the pressure is also high enough to produce plastic deformation. Pressure might lead to shear transformation zones (STZ) [45], i.e. small clusters of particles which experience significant shear. STZ might in turn lead to shear bands [46]. Here evidence for STZs is observed, indicating clearly that the pressure was also high enough to produce plastic deformation. However, the small STZs do not join to form a shear band. In both crystalline and amorphous case, the presence of defects after irradiation might lead to radiation-induced mechanical hardening, provided that defect kinetics at macroscopic times does not destroy them. This is a phenomena studied for collision cascade irradiation [47], but not so much for irradiation in the electronic regime [48].

### b) **Dependence on the effective energy loss**

Figure 5 shows quantitative data on the average crater diameter ($D_{crater}$), crater depth ($Z_{crater}$) and rim volume ($V_{rim}$) for crystalline and amorphous samples as a function of the effective dE/dx. $V_{rim}$ is the volume of the protruded region above the unperturbed surface position around the crater hole. The definitions of the crater dimensions are given in the insets of Figure 5. The analyses were performed using tools available in OVITO [32]. The error bars provided in the figure were estimated taking into account both statistical fluctuations among similar simulations (ran with different random seeds) and uncertainties in the measurements of the crater dimensions. Variations due to the simulations themselves are negligible compared to uncertainties in the crater size measurements, which stems basically from the difficulties of determining the exact point where a given feature begins or ends, and the plane of reference for the unperturbed surface. Measurements were taken in two planes: (100) and (010), corresponding to top and cross-sectional (lateral) views, respectively.

Craters are wider for the amorphous sample, but the crater diameter in both systems shows a square-root dependence with $(dE/dx)_{eff}$. Crater depth, on the other hand first increase sharply with increasing dE/dx (supralinearly in the amorphous and linearly for the crystalline film), but dependence weakens as the physical size of the films ($Z_{crater}=h$) is approached. The depth of the crater reaches the physical limit of the film at energy loss values close to 1 keV/nm in the amorphous films, for the crystalline case, larger dE/dx are required. Thus, crater depth and radius do not scale equally with dE/dx, in contrast to simple scaling laws that predict a roughly hemispherical crater, with each dimension proportional to $(dE/dx)^n$ (with n varying from ½ [49] to 1 [50]).

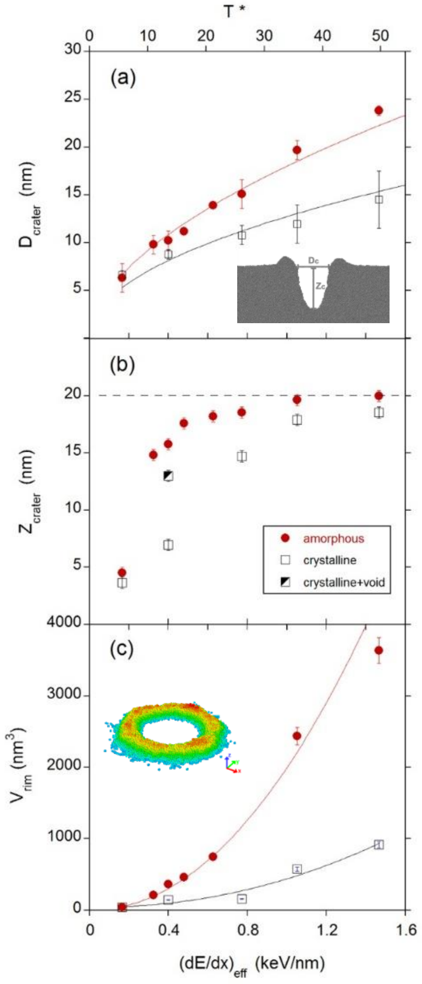

Figure 5. Crater diameter $D_{crater}$ (a), with inset figure of measurements definitions, and depth $Z_{crater}$ (b), and rim volume $V_{rim}$ (c) as function of effective stopping power for amorphous (circles) and crystalline (squares) films with h= 20 nm. Lines for crater diameter are $D_{crater} \sim (dE/dx)_{eff}^{1/2}$, as suggested in [27]. The crater depth curve includes a point where the size of the void below the 'regular' crater was added to compute the total depth and a dashed line indicating the film thickness. Rim volume plots includes $(dE/dx)_{eff}^{2}$ fits (solid lines).

For the crystalline films, in several cases the fast cooling of the crater together with a dense dislocation forest lead to the collapse of crater walls, which formed faceted voids bellow the crater (Supplemental Figure 1 in ref. [37]). For one value of dE/dx, the appearance of voids was particularly pronounced and a point was added in

Figure 5b, showing the value of the cavity depth including the length of the void. Further increase in energy loss did not result in deeper craters (we tested up to 3 keV/nm). This means that the initially non-excited particles of the substrate contribute negligibly to sputtering, later discussed in details, or to the crater shape. Diffusion of the excitation energy to the substrate is also very limited along the axis of the impact during the short time scale for cratering and sputtering.

This scaling is similar to what was obtained previously for a crystalline LJ solid [27]. The rim volume is much larger for the amorphous sample, tough, as for the crater hole, the scaling with $(dE/dx)_{eff}$ is similar for both systems. Curves of $V_{rim}$ is proportional to $(dE/dx)_{eff}^2$ are shown as solid lines in Figure 5. The square dependence scaling is approximate, as it becomes weaker at larger dE/dx, especially for the amorphous case. It is also clear from Figure 5c that there is a minimum or threshold stopping power for rim formation, which is phase dependent. The smallest effective energy loss to observe a distinguishable rim in the amorphous sample is close to 0.15 keV/nm, but ~ 0.7 keV/nm in the crystalline sample, an increase by a factor of four. The lower threshold for the rim formation in the amorphous is attributed to the lower stress threshold for plasticity in this system, as previously discussed (critical stress of 1.5 versus 2.5 for the crystal) and the larger contribution of melt flow to the rim in the amorphous film,

In summary, all crater dimensions tend to be larger in the amorphous targets. As the initial deposited energy is the same in both cases, such differences must be related to the way energy is dissipated and transported out of the excited region after the ion passage. As already pointed out, this is in part due to the higher diffusivities in the crystalline samples, where energy is rapidly diluted in larger volumes. Free volume and particle mobility is also enhanced in the amorphous system facilitating mass transport and melt flow out of the excited region during longer times after the ion excitation. Such differences in energy transport, which impacts the “slower” events of crater formation and relaxation, are, however, not so important for the faster process involved in sputtering, as discussed below.

Figure 6 shows the sputtering yield (Y) as a function of effective stopping power for amorphous and crystalline films of h=20nm. Both crystalline and amorphous targets present nearly identical sputtering yields. Unlike the predictions of quadratic dependence with dE/dx in analytical spike models [14] which neglect pressure and surface effects, the dependence observed here is roughly linear, same as in simulations of infinitely long tracks [24]. This is to be expected as far as most of the ejection depth is smaller than film thickness.

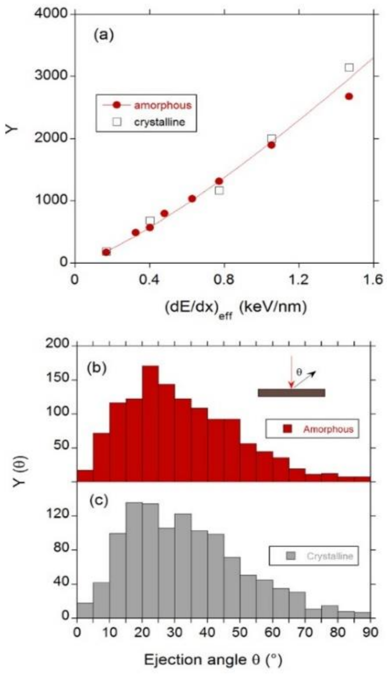

Figure 6. Comparison of sputtering from amorphous and crystalline LJ films (h=20nm) for an excited track of $R_{track}$=3 nm. (a) Yield of sputtered particles as function of effective stopping power for amorphous and crystalline films. A fit with a power of 1.2 is included, as suggested from simulations of infinitely long tracks [24] (b) Exit angle distribution of sputtered particles from crystalline and amorphous samples in the case of $(dE/dx)_{eff}$=0.77 keV/nm (T*=25). The average exit angle is very similar in both cases: 33±19° for the crystalline films and 32±19° for the amorphous, where the uncertainty is the standard deviation of the population. The standard error for the mean is ~0.5°.

The exit angle distribution of sputtered atoms at one fixed dE/dx is also shown in Figure 6. Surprisingly, the amount of ejected particles and the mean sputtering angle (33±19°) were very similar in both systems, crystallinity having no influence in this matter. We attribute such similarity to the extremely high temperature and disordered condition of the track region from where most ejected particles originate, as indicated by the arrows in Figure 3.

The amount of sputtered particles in our simulations was significantly smaller than the number of particles corresponding to the crater volume, as already noted previously [24, 27]. This is in part due to melt flow and redeposition at the crater rims of highly excited particles of the spike and to the particles that are pushed radially towards the walls of the crater, where they accommodate in a compacted region. Both effects are clearly seen in the movie provided in the supplemental material [37]. For thick films, the number of sputtered particles is 30-50% smaller than the number of particles in the rim.

### c) **Thickness dependence**

In this section we discuss how surface effects change with decreasing film thickness. In the following, we concentrate our discussion in the amorphous case that has a morphology very similar to the experimental craters in amorphous organic films, used here for comparison. In Figure 7, top-view, AFM-like pictures of MD craters are shown for different film thicknesses *h*. In this set of simulations, LJ samples were excited by a spike with T*=25 and the initial track radii was $R_{track}$=3 nm. We chose on purpose MD initial track conditions in the amorphous LJ films that give a reasonable agreement with crater diameters seen on PMMA films [25] bombarded by 923 MeV Pb ions [$(dE/dx)_{el}$ close to 15 keV/nm], shown in Figure 7. For qualitative purpose, we also added images of crater for varying thickness crystalline films in Figure 7, but those simulations were run with $R_{track}$=2 nm.

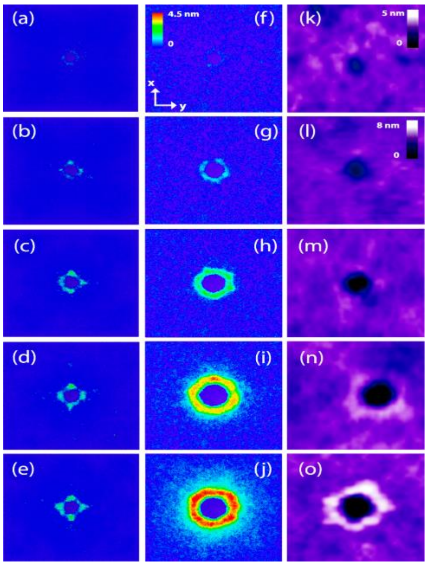

Figure 7. Comparison of experimental craters produced by swift heavy ions in PMMA with simulated craters in crystalline and amorphous LJ films. Top view, AFM-like images of simulated craters (T*=25, R=3 nm) for (a-e) crystalline and (f-j) amorphous films of different thicknesses: (a) 2.5 nm; (b) 3.5 nm; (c) 8.5 nm; (d) 18.5 nm; (e) 43.5 nm; (f) 2 nm; (g) 3.6 nm; (h) 6.6 nm; (i) 20 nm; (j) 43 nm. Right row depicts (k-o) AFM images of craters produced by 923 MeV Pb in PMMA thin films of thicknesses (k) 2 nm; (l) 4 nm; (m) 8 nm ; (n) 20 nm (o) 42 nm. The images size is 80×80 $nm^2$ for all cases.

Under the conditions described above, MD crater diameters in the amorphous films are ~25% smaller than those measured experimentally. However, MD rim volumes and crater depths are substantially larger than experimental ones, reflecting the much weaker bonding of a LJ system, compared to entangled polymer chains of real films. For example, simulated rim volumes are a factor of four larger. Despite such quantitative disagreement (expected in such a simple model), the simulations mimic very well the dependence of crater diameter and rim volume with thickness seen in the experiments. Starting from a saturation value at thick layers, the rim size remains unchanged down to a thickness of ~30 nm, followed by steep decrease for thinner layers. A similar condition is observed for the thickness dependence of crater´s radii, but the critical thickness below which thickness-dependent effects starts is shifted to approximately h<10 nm and the shrinking of the crater hole with h is less steep. This decrease in crater and rim dimensions fits very well to theoretical predictions of models for which radiation effects at the surface are driven by the sum of elementary excitations along the track [40, 25]. Such cooperative action becomes naturally weaker for shorter track lengths. In the simulations, the pressure pulse is weaker and cooling of the excited track is more efficient in short tracks, both contributing to the decreased radiation damage efficiency on ultrathin layers. Long-range effects along the track are particularly critical to the rim formation. This is reflected in the much larger critical thickness where deviations from bulk behavior start to be observed.

There are also some important aspects to note, concerning the dependence of crater depth with thickness. The depth of simulated craters in a-LJ films followed the curve $Z_{crater}=h$ for h values up to h~30nm. Even for the thickest film tested (60 nm) crater depth is far from reaching a saturation value, typically seen in the experiments [10, 25]. Obviously when the thickness of the sample is equivalent to or below the maximum (saturation) $Z_{crater}$, the depth of the crater starts to become physically limited by the thickness and $Z_{crater}=h$ is a natural possibility at small $h$. However, experimentally, crater depth does not follows the curve $Z_{crater}=h$ even when the thickness is smaller than the saturation crater depth [25], contrary to what is seen in the simulations. Simulated craters are deeper, not because sputtered particles comes from deep layers, but because of a large contribution from melt flow in a LJ material. As seen in Figure 3d, many hot particles move upwards from the inner regions of the track and are deposited at the rim region.

In fact, in the simulations, sputtering yield is dominated by particles originally lying above $z=h/2$, even in very thin films. Figure 8 shows the distribution of the depth of origin of ejected particles for films of thickness h of 2 and 20nm and the fraction of ejected particles originating from $z<h/2$ for all thickness tested. For the 2nm film, ~ 94% of the ejected particles comes from $z<h/2$. For the other thicknesses, this fraction is even larger. The h/2-limitation for the depth of origin of ejected particles from thin films can be understood noting that momentum transfer is critical for particle ejection. In the simulations, the z-component of the velocity of excited particles tend to be positive (i.e., points toward the surface) only for particles located at a position with $z<h/2$. This is clearly seen in Figure 3c and d, where displacement vectors from initial positions have upward arrows starting near z=h/2. Below that depth, displacements have a high degree of randomness, or tend to point downwards. Such observations are also in agreement with predictions by analytical models based on sum of impulses [18, 40]. According to this model, in a film with a finite thickness, the total impulse transmitted to a particle in the film points upward only if it is located at a position with $z<h/2$. At points with $z>h/2$ the impulse direction is inverted and push particles towards the substrate.

Total sputtering yield also experience a drop with film thinning (Figure 8a), occurring at the same thickness than the drop for rim volume, and indicating a connection between the two events. Angular distribution of ejected particles, on the other hand, is not much affected by thickness reduction. For thinner films, both the pressure pulse and melt flow are reduced, and cratering/sputtering is mostly due to rapid phase explosion, as for bombardment of large clusters [34].

The fact that many experimental trends are reproduced with the simple LJ film/substrate model used here, implies that crystalline Si in the experiments acts to a good approximation as a non-excitable substrate, as in the simulations (this may not be the case for amorphous Si, however [51]). We already pointed out that exchange of energy between particles at the bottom of the track and the initially non-excited particles is small. Indeed, exciton diffusion lengths in polymers are expected to be around 1-3 nm and would only be relevant for the thinnest films considered here. Diffusion under the non-equilibrium conditions produced by the track might lead to significantly different values for exciton diffusion, but our results suggest that this is not the case and excitation decay occurs rapidly. Therefore, for film thickness larger than about 10 nm, we predict that using an insulating or metallic substrate would lead to similar surface features. Using polymers with much larger exciton diffusion length (for instance due to chain bonding or doping) might still lead to the same scenario, provided excitation coupling to the atomic cores is fast enough.

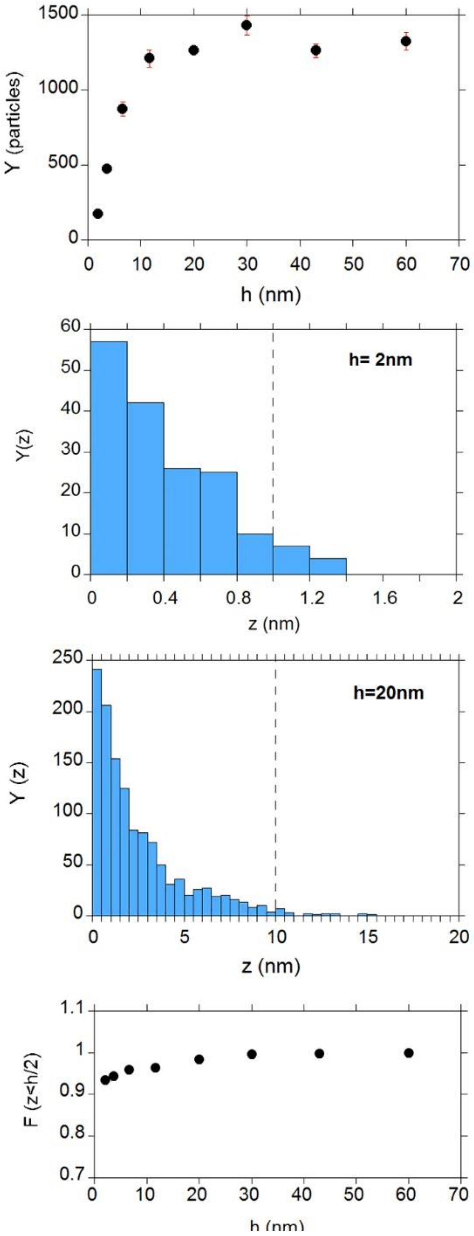

Figure 8. Sputtering yield and depth of origin of ejected particles as a function of h. (a) Total sputtering yield as a function of thickness for R=3 nm and T*=25. (b-c) Distribution of the number of puttered particles as a function of the depth of origin z for a 2 nm and a 20 nm thick films. (d) Fraction of ejected particles originating from depths *z<h/2* for various film thicknesses.

## Conclusions and summary

To summarize, surface modification by electronic excitations produced in nanometer-thick LJ films with amorphous structure to better mimic a polymer film, are controlled by the excitation in the film itself, with negligible substrate effects. Crater formation is controlled by track size and temperature, with crater size being mostly determined by evaporation and melt flow from the hot track. The rim size is determined both by melt flow and by coherent displacement of particles, due to the large pressure developed in the excited track. Craters and rims are much larger in amorphous films essentially due to the slower cooling of the excited region, compared to fast cooling in the crystalline matrix due to energy transport along close-packed directions. This also results in an effective threshold stopping power for rim formation which is appreciably larger in the crystalline sample. On the other hand, sputtering yields from both crystalline and amorphous samples are similar (including the angular dependence), indicating that ejected particles arise mostly from the highly excited track, making the initial phase structure of the material not relevant.

We found a large dependence of surface effects on film thickness below a critical value, which is different for crater diameter and for rim volume, due to the different mechanisms involved in each case. In the simulations, crater diameter is sensitive to film thickness only for $h<10$ nm. The rim volume is more sensitive to thickness effects ($h<30$nm), because its formation is partly due to a pressure pulse effect requiring a coordinated push from depth to lift surface platelets.

Here we employed a very simple model of particles interacting via LJ potentials in tracks of variable length to simulate cratering in thin films of organic materials and, in particular, polymers. Generating and irradiating large samples ($>10^6$ particles) with polymer chains simulated with FENE [52] or more complex interactions, like the Brenner´s potential, would be an obvious improvement to simulate a “real” polymer in future work. Other simulation configurations that better model the role of the substrate can also be employed, including (a) using a 2-type LJ system to mimic different mechanical properties of film and substrate; (b) adding exciton quenching; or (c) adding electronic heating for insulating substrates with different temperature and heating times. This will for sure improve quantitative agreement with cratering features in real experiments. However, we demonstrate that several important features observed in experiments with macromolecular thin films are already reproduced by amorphous LJ samples, showing the usefulness of simple potentials to simulate complex organic materials perturbed by high-energy ions.

## Acknowledgements

We thank discussions with R. Gonzales-Valdez, V. de Menezes, and D. Tramontina. E.M.B. Expresses thanks for support from SeCTyP-UNCuyo under Grant No. M003, and ANPCyT under Grant No. PICT-2014-0696. This work is part of the IAEA Coordinated Research Project on Development of molecular concentration mapping techniques using MeV focused ion beams, CRP F11019 (Contract 18352/R0 and )

## References

[1] A. Meftah, F. Brisard, J. M. Costantini, E. Dooryhee, M. Hage-Ali, and M. Hervieu, Phys. Rev. B **49,** 12457 (1994) doi: http://dx.doi.org/10.1103/PhysRevB.49.12457

[2] M. Toulemonde, W. Assmann, C. Dufour, A. Meftah, and C. Trautmann, Nucl. Instrum. Methods Phys. Res. B **277** (2012) doi: http://dx.doi.org/10.1016/j.nimb.2011.12.045

[3] R. L. Fleischer, P. B. Price, and R. M. Walker, in *Nuclear Tracks in Solids: Principles and Applications* (University of California Press, 1975).

[4] M. Toulemonde, W. Assmann, C. Trautmann, and F. Grüner, Phys. Rev. Lett. **88**, 057602 (2002) doi: http://dx.doi.org/10.1103/PhysRevLett.88.057602

[5] R. D. Macfarlane and D. F. Torgerson, Phys. Rev. Lett. **36**, 486 (1976) doi: http://dx.doi.org/10.1103/PhysRevLett.36.486

[6] H. Dammak, A. Dunlop, and D. Lesueur, Philos. Mag. A, **79**, 147 (1999) doi: 10.1080/01418619908214280

[7] R. M. Papaléo, M. R. Silva, R. Leal, P. L. Grande, M. Roth, B. Schattat, G. Schiwietz, Phys. Rev. Lett. **101**, 167601 (2008) doi: http://dx.doi.org/10.1103/PhysRevLett.101.167601

[8] J. Kopniczky, C. T. Reimann, A. Hallén, B. U. R. Sundqvist, P. Tengvall, and R. Erlandsson, Phys. Rev. B **49**, 625 (1994) doi: http://dx.doi.org/10.1103/PhysRevB.49.625

[9] D. Schwen, E. Bringa, J. Krauser, A. Weidinger, C. Trautmann, and H. Hofsäss, Appl. Phys. Lett. **101**, 113115 (2012) doi: http://dx.doi.org/10.1063/1.4752455

[10] R. M. Papaléo, L. S. Farenzena, M. A. de Araújo, R. P. Livi, M. Alurralde, and G. Bermudez, Nucl. Instrum. Methods Phys. Res. B **148**, 126 (1999) doi: 10.1016/S0168-583X(98)00877-5

[11] O. Ochedowski, *et al.* Nat. Commun. **5 (**2014) doi: 10.1038/ncomms4913

[12] H. M. Urbassek, Nucl. Instrum. Methods Phys. Res. B **122**, 427 (1997) doi: 10.1016/S0168-583X(96)00681-7

[13] R. E. Johnson and R. Evatt, Radiat. Eff. **52**, 187 (1980) doi: 10.1080/00337578008210031

[14] P. Sigmund and C. Claussen, J. Appl. Phys **52**, 990 (1981) doi:

http://dx.doi.org/10.1063/1.328790

[15] G. Szenes, K. Havancsák, V. Skuratov, P. Hanák, L. Zsoldos, and T. Ungár, Nucl. Instrum. Methods Phys. Res. B **166**, 933 (2000) doi: 10.1016/S0168-583X(99)00733-8

[16] I. S. Bitensky and E. S. Parilis, Nucl. Instrum. Methods Phys. Res. B **21**, 26 (1987) doi: 10.1016/0168-583X(87)90135-2

[17] L. E. Seiberling, J. E. Griffith, and T. A. Tombrello, Radiat. Eff. **52**, 201 (1980) doi: 10.1080/00337578008210033

[18] D. Fenyö and R. E. Johnson, Phys. Rev. B **46**, 5090 (1992) doi: http://dx.doi.org/10.1103/PhysRevB.46.5090

[19] M. M. Jakas, E. M. Bringa, and R. E. Johnson, Phys. Rev. B **65**, 165425 (2002) doi: http://dx.doi.org/10.1103/PhysRevB.65.165425

[20] R. Devanathan, P. Durham, J. Du, L. R. Corrales, and E. M. Bringa, Nucl. Instrum. Methods Phys. Res. B **255**, 172 (2007) doi: 10.1016/j.nimb.2006.11.021

[21] O. H. Pakarinen, F. Djurabekova, K. Nordlund, P. Kluth, and M. C. Ridgway, Nucl. Instrum. Methods Phys. Res. B **267**, 1456 (2009) doi: 10.1016/j.nimb.2009.01.071

[22] P. Kluth, C. S. Schnohr, O. H. Pakarinen, F. Djurabekova, *et. al.* Phys. Rev. Lett. **101**, 175503 (2008) doi: http://dx.doi.org/10.1103/PhysRevLett.101.175503

[23] E. M. Bringa and R. E. Johnson, Surf. Sci. **451**, 108 (2000) doi: 10.1016/S0039-6028(00)00015-7

[24] E. M. Bringa, R. E. Johnson, and M. Jakas, Phys. Rev. B*,* vol. **60**, 15107 (1999) doi: dx.doi.org/10.1103/PhysRevB.60.15107

[25] R. M. Papaléo, R. Thomaz, L. I. Gutierres, V. M. de Menezes, D. Severin, C. Trautmann*, et al.*, Phys. Rev. Lett. **114**, 118302 (2015) doi: http://dx.doi.org/10.1103/PhysRevLett.114.118302

[26] E. M. Bringa, K. Nordlund, and J. Keinonen, Phys. Rev. B **64**, 235426 (2001) doi: http://dx.doi.org/10.1103/PhysRevB.64.235426

[27] E. M. Bringa, R. E. Johnson, and R. M. Papaléo, Phys. Rev. B **65**, 094113 (2002) doi: http://link.aps.org/doi/10.1103/PhysRevB.65.094113

[28] E. M. Bringa and R. E. Johnson, Nucl. Instrum. Methods Phys. Res. B **193**, 365 (2002) doi: 10.1016/S0168-583X(02)00806-6

[29] S. Plimpton, J. Comput. Phys. 117, **1** (1995) doi: doi:10.1006/jcph.1995.1039

[30] E. M. Bringa and R. E. Johnson, Nucl. Instrum. Methods Phys. Res. B **143**, 513 (1998) doi: 10.1016/S0168-583X(98)00405-4

[31] G. Szenes, Nucl. Instrum. Methods Phys. Res. B **116**, 141 (1996) doi: 10.1016/0168-583X(96)00025-0

[32] S. Alexander, Model. Simul. Mater. Sci. Eng. **18**, 015012 (2010).

[33] R. M. Papaléo, R. Leal, W. H. Carreira, L. G. Barbosa, I. Bello, and A. Bulla, Phys. Rev. B **74**, 094203 (2006) doi: http://dx.doi.org/10.1103/PhysRevB.74.094203

[34] C. Anders, E. M. Bringa, F. D. Fioretti, G. Ziegenhain, and H. M. Urbassek, Phys. Rev. B **85**, 235440 (2012) doi: http://dx.doi.org/10.1103/PhysRevB.85.235440

[35] C. Anders, E. M. Bringa, G. Ziegenhain, G. A. Graham, J. F. Hansen, N. Park, *et al.* Phys. Rev. Lett. **108**, 027601 (2012) doi: http://dx.doi.org/10.1103/PhysRevLett.108.027601

[36] M. Ghaly and R. S. Averback, Phys. Rev. Lett. **72**, 364 (1994) http://dx.doi.org/10.1103/PhysRevLett.72.364

[37] "See Supplemental material at [url to be provided] for further details on the crater evolution for the molecular dynamics simulations of crystalline and amorphous samples.".

[38] E. M. Bringa, R. E. Johnson, and Dutkiewicz, Nucl. Instrum. Methods Phys. Res. B **152**, 267 (1999) doi: http://dx.doi.org/10.1103/PhysRevB.60.15107

[39] K. Nordlund, J. Keinonen, M. Ghaly, and R. S. Averback, Nature **398**, 49 (1999) doi: 10.1038/17983

[40] R. E. Johnson, B. U. R. Sundqvist, A. Hedin, and D. Fenyö, Phys. Rev. B **40**, 49 (1989) doi: http://dx.doi.org/10.1103/PhysRevB.40.49

[41] E. M. Bringa, E. Hall, R. E. Johnson, and R. M. Papaléo, Nucl. Instrum. Methods Phys. Res. B **193**, 734 (2002) doi: 10.1016/S0168-583X(02)00895-9

[42] Y. Gao, C. J. Ruestes, D. R. Tramontina, and H. M. Urbassek, J. Mech.Phys. Solids **75**, 58 (2015) doi: 10.1016/j.jmps.2014.11.005

[43] D. J. Quesnel, D. S. Rimai, and L. P. DeMejo, Phys. Rev. B **48**, 6795 (1993) doi: http://dx.doi.org/10.1103/PhysRevB.48.6795

[44] P. Cao, X. Lin, and H. S. Park, J. Mech. Phys. Solids **68**, 239 (2014) doi: 10.1016/j.jmps.2014.04.004

[45] C. A. Schuh and C. Lund, Nat. Mat. **2,** 449 (2003) doi: 10.1038/nmat918

[46] F. Shimizu, S. Ogata, J. Li, Acta Materialia **54**, 4293 (2006) doi: 10.1016/j.actamat.2006.05.024

[47] T. Diaz de la Rubia, *et. al.* Nature **406**, 871 (2000) doi:10.1038/35022544

[48] Charnvanichborikarn, S. Worsley, S. M. A. Shin, S. J. Kucheyev, S. O. Carbon **57**, 310 (2013) doi: 10.1016/j.carbon.2013.01.078

[49] I. S. Bitensky, E. S. Parilis, Nucl. Instrum. Methods Phys. Res. B **21**, 26 (1987) doi:10.1016/0168-583X(87)90135-2

[50] R. E. Johnson, B. U. R. Sundqvist, A. Hedin, and D. Fenyö, Phys. Rev. B **40**, 49 (1989) doi: http://dx.doi.org/10.1103/PhysRevB.40.49

[51] T. Bierschenk, R. Giulian, B. Afra, M. D. Rodriguez, *et. al.* Phys. Rev. B **88**, 174111 (2013) doi: http://dx.doi.org/10.1103/PhysRevB.88.174111

[52] K. Kremer and G. S. Grest, J. Chem. Phys. **92**, 5057 (1990) doi: http://dx.doi.org/10.1063/1.458541

# Supplemental Material for “Simulations of cratering and sputtering from an ion track in crystalline and amorphous Lennard Jones thin films”

## 1. Crater Evolution

Suppl. Fig. 1 shows several snapshots of the crater evolution - lateral view of a thin slice in the center of the plane (010) - for a 20 nm thick amorphous and crystalline films (left and right columns, respectively) after perturbation by an ion track with radius $R_{track}$=3nm and temperature ($T_{LJ}$) of 25 LJ units. The displayed time range is from 9 ps up to 70 ps. It is possible to track down the dissipation of the energy released by the hot track to the unperturbed matrix resulting in the ejection of energetic particles, cratering and relaxation. The color code represents particle kinetic energy (KE), where blue stands for particles with associated KE under the fusion temperature, and red stands for particles with associated KE above the vaporization temperature. Any other color stands for a temperature range in the melt phase.

While for the amorphous film the energy dissipates in a cylindrical symmetry, the crystalline film dissipates energy in preferential directions along its crystallographic planes, allowing the energy to fade up faster. At the 19 ps snapshot, for example, it is possible to see a larger energy density close to the ion track in the amorphous film when compared to the crystalline case. The slower energy dissipation in the amorphous sample leads to the formation of a larger molten region, which ends up producing wider and deeper craters, once the particles of this region have greater mobility when compared to the solid particles (in blue). On the other hand, the quickness of the relaxation processes described in the crystalline sample may cause the formation of a void below the crater, as can be seen in Suppl. Fig. 1 (h).

This scenario may also be appreciated in the movie provided (Suppl. Movie 1), where the evolution of the system is shown through the displacement vectors of the particles from their original positions. The movie presents a lateral view of a thin slice in the center of the plane (010) in an amorphous film with thickness h=20 nm excited by a track with $R_{track}$=3nm and $T_{LJ}$=25. The video encompasses a time range of 190 ps after the perturbation by the ion and is composed by 237 frames. The movie clearly shows the following features: 1) most of the sputtering occurs in short times, with the majority of ejected particles coming from a depth $z \leq h/2$; 2) melt flow (longer arrows) transporting particles to the top of the rim); 3) coherent displacement of particles pushing material upwards to form the first layers of the rim, and 4) the compaction of particles in the walls of the crater due to the radial expansion of the heated track.

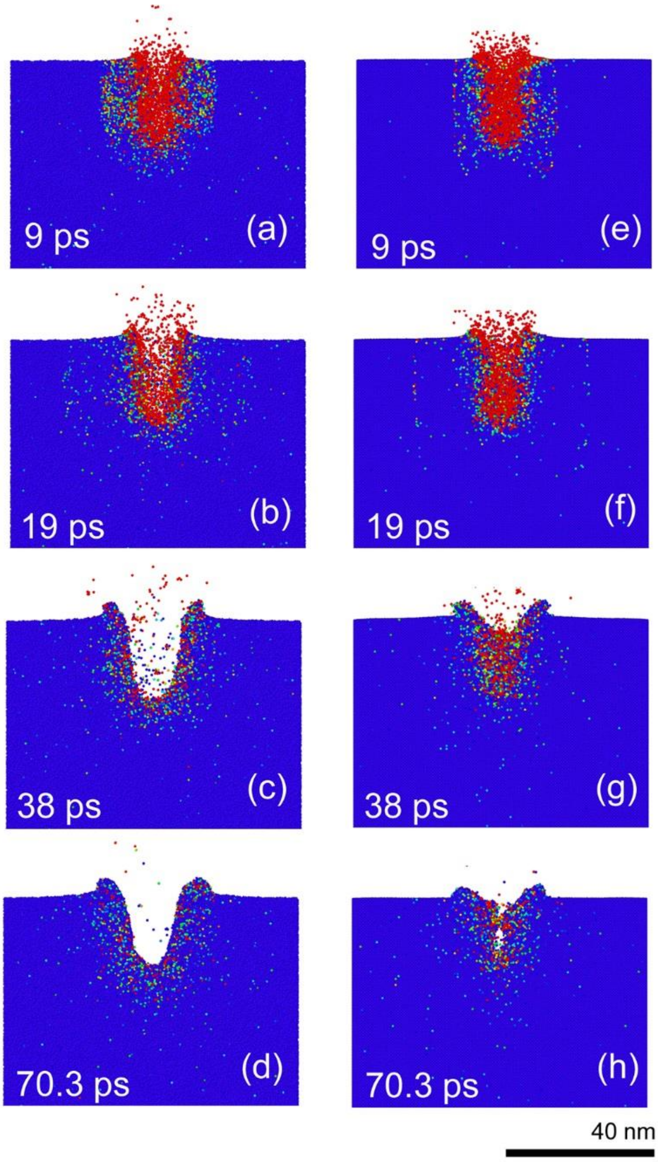

**Supl Figure 1.** Crater evolution for 20 nm thick amorphous (a-d) and crystalline (e- h) films excited with a spike with $R_{track}$=3nm and $T_{LJ}$=25. The color code represents particle kinetic energy (KE) (blue stands for particles with associated KE under the fusion temperature and red stands for particles with associated KE above the vaporization temperature, any other color stands for a temperature range in the melt phase).

# 4. SEGUNDO ARTIGO ORIGINAL

## Molecular dynamics simulation of polymer-like thin films irradiated by fast ions: a comparison between FENE and Lennard-Jones potentials

N. W. Lima[1], L. I. Gutierres[1], R. I. Gonzalez[2], S. Müller[1], R.S.Thomaz[1], R. M. Papaléo[1] and E. M. Bringa[3]

1 Faculdade de Física PUCRS, Av. Ipiranga, 6681, 90619-900 Porto Alegre, Brazil

2 Departamento de Física, Facultad de Ciencias, CEDENNA, Universidade de Chile, Casilla 653 Santiago 78000024, Chile

3 Facultad de Ciencias Exactas y Naturales Universidad Nacional de Cuyo, Mendoza, Argentina

### ABSTRACT

In this work, surface effects of individual heavy ion impacting thin polymer-like films were investigated using molecular dynamics simulation (MDS) with the FENE potential to describe the molecular chains. The perturbation introduced by the ions in the lattice was modeled assuming that the initial excitation energy in the ion track is converted into an effective temperature, as in a thermal spike. The track was heated only within the film thickness *h* (varied from 2-60 nm), leaving bellow a non-excited substrate. The effect of a decreasing thickness on cratering and sputtering was evaluated. The results were compared to experimental data of thin polymer films bombarded by MeV-GeV ions and to simulations performed with the Lennard-Jones potential. While several qualitative results observed in the experiments were also seen in the simulations, irrespective of the potential used, there are important differences observed on FENE films. Crater size and sputtering yields are substantially reduced in FENE simulations. This is attributed to the additional restrictions to mass transport out of the excited track

region imposed by interchain interactions (entanglements) and by the low mobility of the molten phase induced by the spike. Overall, there is a better agreement between MDS and experiments for the FENE than for the LJ potential.

## 1. Introduction

High-energy charged particles have been widely used to characterize and modify materials in a controlled way, leading to important applications in different fields of materials science and engineering, medicine and geosciences [1–4]. Sufficiently fast ions deposit a large amount of localized electronic excitation along its path through the material, which can be coupled to the lattice [5] and produce radiation damage in the bulk [2], sputtering and mass transport at the near surface [6]. In particular, for polymers and other organic materials, radiation effects of swift heavy ions are very pronounced, involving complex and irreversible chemical rearrangements along the ion path and large yield of particle emission. Sputtering in the electronic stopping regime is very efficient for organic materials [2,7] and large craters are often found at the point of ion incidence [7, 8, 9].

Because of that, the use of electronic sputtering for characterizing organic materials has gained especial attention in recent years [10, 11]. This stems from the fact that secondary ion mass spectrometry with MeV-ions (MeV-SIMS) shows higher sputtering yields and less molecular fragmentation, when compared to keV-SIMS, and it is capable of molecular mapping of samples, including of tissues at high pressure atmospheres [11–13]. Even though several basic aspects of electronic sputtering have already been clarified since the early works in the field [14, 15], many mechanistic details, important for mass spectrometry applications, are still not well understood [16]. One example is the complex and transient processes of energy deposition and transport leading to sputtering, which are not easily accessed via experimental observations. In this respect, there are important gaps that only computer simulations can provide adequate inputs. This includes details of the fast (femtosecond) energy transport by secondary electrons using Monte Carlo (MC) simulations [17], or tracking the subsequent dynamics (on a nanosecond time scale) of the atoms set in motion by MD simulations [18–25].

To simulate non-equilibrium energy transport and sputtering from ion tracks in molecular solids, the simplest approach is to employ the Lennard-Jones (LJ) potential, suited to model van der Waals solids such as condensed gases [19, 26, 27]. LJ has been also applied to explain several features of the electronic sputtering of biomolecules in the pioneering work of Fenyö et al. [28], and later to describe cratering in polymers as a function of the excitation density in the tracks [29, 30]. More recently, simulations with LJ have also been used to evaluate the effect of spatial confinement of ion tracks on cratering and sputtering of ultrathin polymer films irradiated by swift ions, with good qualitative agreement with experimental observations [31]. Despite the low computational cost associated to the Lennard-Jones potential, there are limitations on the simulation predictions, which stems from the oversimplifications of the model.

In this paper, we extend our previous simulations of surface effects caused by the impact of individual swift heavy ions on LJ thin films [29], by explicitly including a molecular chain. We chose to simulate a polymer chain at the coarse-grained level, in which each monomer is represented as a particle bound to its neighbors via a FENE (Finite Extensible Nonlinear Elastic) potential [32]. The FENE potential has been successfully used to investigate viscoelastic and rheological properties of polymers and their dependence on chain length [33–35]. Other coarse grained models have been already used for studying effects of radiation in polymers but only at the low ion energy range [36, 37], where nuclear collisions dominate. Overall, we observe better agreement between experiments and simulation using the FENE potential, for which craters, sputtering yields and flow of molten material are substantially reduced, as compared to the LJ system.

## 2. MD simulations

Classical molecular dynamics simulations were performed using LAMMPS (Large-scale Atomic/Molecular Massively Parallel Simulator) [38] with conditions similar to what has been applied in previous simulations of cratering in polymers [29, 31, 39]. Polymer molecules were modeled as a chain of monomers with intrachain bonds governed by the FENE potential and interchain interactions modeled by LJ potential. Lennard-Jones and FENE potentials are given in equation 1 and 2, respectively:

$$\boldsymbol{E_{LJ}} = \boldsymbol{4\epsilon}[\left(\frac{\sigma}{r}\right)^{\boldsymbol{12}} - \left(\frac{\sigma}{r}\right)^{\boldsymbol{6}}] \tag{1}$$

$$\boldsymbol{E_{FENE}} = -0.5KR_0{}^2 \ln\left[1 - \left(\frac{r}{R_0}\right)^2\right] + \boldsymbol{4\epsilon}\left[\left(\frac{\sigma}{r}\right)^{\boldsymbol{12}} - \left(\frac{\sigma}{r}\right)^{\boldsymbol{6}}\right] + \epsilon \tag{2}$$

In both equations, σ has space units, ϵ has energy units and $r$ is the interatomic distance. In the FENE potential, $R_0$ indicates the maximum distance allowed between monomers directly bonded in the same chain and $K$ has energy/space$^2$ units and it corresponds to the elastic constant of the system for small interatomic distances. The parameters used for both potentials are described in Table 1. Note that in the FENE construction, as $r \to R_0$; $E_{FENE} \to \infty$, which hinders adjacent particles in a chain to move farther than $R_0$. This means that radiolytic processes such as chain scission, production of small fragments and bond rearrangements observed in real organic materials are not allowed in our simulations. Thus, LJ and FENE approaches correspond to two extreme cases of weakly and very strongly bonded chains.

Table 1 Parameters used for LJ and FENE potentials

| Parameter | Value | |
|---|---|---|
| | Physical units | LJreduced unities |
| $\sigma$ | 0.5 nm | 1 |
| $\epsilon$ | 0.07 eV | 1 |
| τo | 1.7 ps | 1 |
| $R_T$ | 3 nm | 6 |
| K | 1.3 N/m | 30 |
| $R_0$ | 0.75 nm | 1.5 |

The simulation boxes contained about 5 million particles within a volume of 80x80x80 nm$^3$, including particles of the film and substrate. The boxes were centered at the origin and had a top free surface perpendicular to the $z$ axis. All other surfaces included a region of Langevin thermostating and damping with a thickness of 2□. Periodic boundary conditions were used in $x$ and $y$ directions (spatial coordinates are defined in Fig. 1).

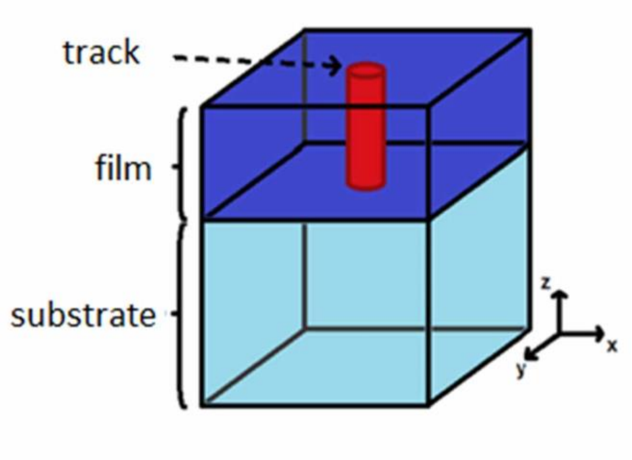

Figure 1. Scheme of film, substrate and ion track. Ion track is parallell to z-axis and normal to the surface.

The interchain potential parameters, σ =0.5 nm and ϵ = 0.07 eV, followed those values previously used to simulate cratering on pure LJ films [29, 31, 39]. Chains containing a hundred monomers were used, each monomer represented as a particle with a mass of 1.66 x $10^{-22}$ g (100 u). This corresponds to a chain of PMMA with $M_W$=10,000 u. Fig. 2 shows the position of 50 molecules in the beginning of a simulation, where it is possible to see that several chains are entangled. Entanglements provide additional constraints to molecular motion, as in a real polymer [37]. The mean radius of gyration was about 2 nm. The amorphous LJ samples were obtained following the methodology described in [20]. The non-cristallinity of both FENE and LJ samples was verified by evaluating the radial distribuition function. The surface of the LJ samples were almost atomically flat, but FENE samples had a natural roughness, with root mean square values around 0.25 nm (Fig.2b-c), close to the values found for polymer thin films on Si substrates by atomic force microscopy.

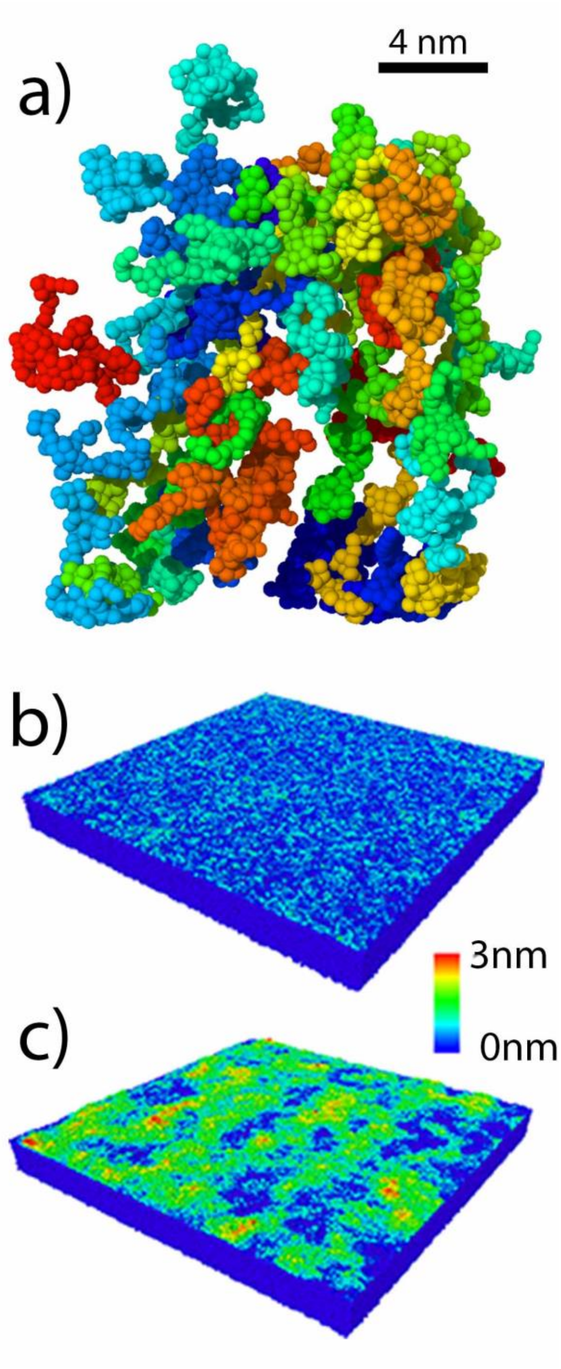

Figure 2. a) Representation of 50 molecules in the FENE sample (each molecule is painted with a different collor). b) Lennard-Jones film and c) FENE film before the thermal spike. A collor code for surface height was used. It is possible to identify that FENE sample presents a greater roughness than LJ sample.

In order to describe the energy deposition by the ion, a thermal spike model was used, as decribed previously [21]. Particles within a radius of 3 nm from the impact point were heated (in about 0.4 ps) by giving them energies corresponding to a temperature of 25,000 K. This forms a region equivalent to the ion track core. The simulations then followed the evolution of the system for about 300 ps, when crater features were already stabilized. The amount of energy deposited in the system per unit length (i.e. the effective stopping power) was evaluated computing the difference in mechanical energy (kinetic plus potential) of the track atoms before and immediately after the heating process was completed, divided by the track length. The effective stopping power, $(dE/dx)_{eff}$ , gives the portion of the total electronic dE/dx that is converted into atomic motion (usually assumed to be around 10-40%) [20, 40]. The $(dE/dx)_{eff}$ associated with the initial track temperature of 25,000 K is ~1 keV/nm. This was the value used previously for Lennard-Jones potentials, which gave a good agreement with experimental data on PMMA thin films [31]. We note that, in order to follow a thermal spike with FENE samples it was necessary to introduce variable timesteps during the simulations. Such approach is justified by the large initial excitation energy, which tends to make the interparticle distance in a chain $r$ close to $R_0$ in the beginning of the simulations, leading to divergences and integration errors. By making smaller time steps when the system was very hot, we could guarantee that no particle would move farther than a reference limit, keeping the simulation stable, while it evolves toward thermal equillibrium.

To model a thin film, the particles were labeled as belonging to the film or the substrate according to their initial depth within the sample (Fig. 1). The track was heated only within the film thickness (i.e. the film thickness is the excited track length). Thus the substrate behaves as a material non-excitable by the fast ions. This is a reasonable assumption for substrates made of Silicon, where ion tracks are not observed. The simulated films have thicknesses *h* in the range of 2 to 60 nm.

The MD output files were analyzed using OVITO [41]. Different cases were simulated three times using different seeds in the velocity distribuition function in order to evaluate statistical fluctuations. Also, the measurement of radiation-induced topological features were performed three times in different plane views in order to take geometrical variations also into account.

## 3. Results

Fig.3 shows the evolution of a ultrathin (5 nm) and a thick (50 nm) FENE films, by looking at a slice in the middle of the simulation box. For comparison, similar results obtained for a 50 nm thick LJ film are also shown in the Fig.3. A color code for kinetic energy was employed, where red depicts particles with kinetic energies higher than the vaporization temperature and blue particles below melting conditions. For comparison purposes, melting and vaporization temperatures obtained for the LJ system were also kept in the FENE images. The different stages of energy dissipation and transport, particle emission, crater formation and relaxation are shown in Figure. There are important differences in the system evolution between the ultrathin and the thick film. For the ultrathin film, almost only the initially excited region of the track is melted and vaporized. There is a slight radial expansion of the vaporized zone (from 3 to 5 nm, Fig. 3a-b), and after 29 ps, when energy dissipation by sputtering is seen, a molten region of ~4 nm is formed. In this case, a rimless crater is formed with the film cooling down very quickly. For the thick film, after about 4 ps a vaporized phase coexists with a much larger molten region extending radially up to ~16 nm (four times larger than in the 5 nm thick film). The vaporized region expands also to larger radius reaching ~7 nm. At ~30 ps, a hole with a depth of ~20 nm is formed, but a subsequent flow of molecules into the cavity reduces substantially the final depth of the crater. It is very clear that the excited region and neighborhoods are kept hot for much longer times in the thick films.

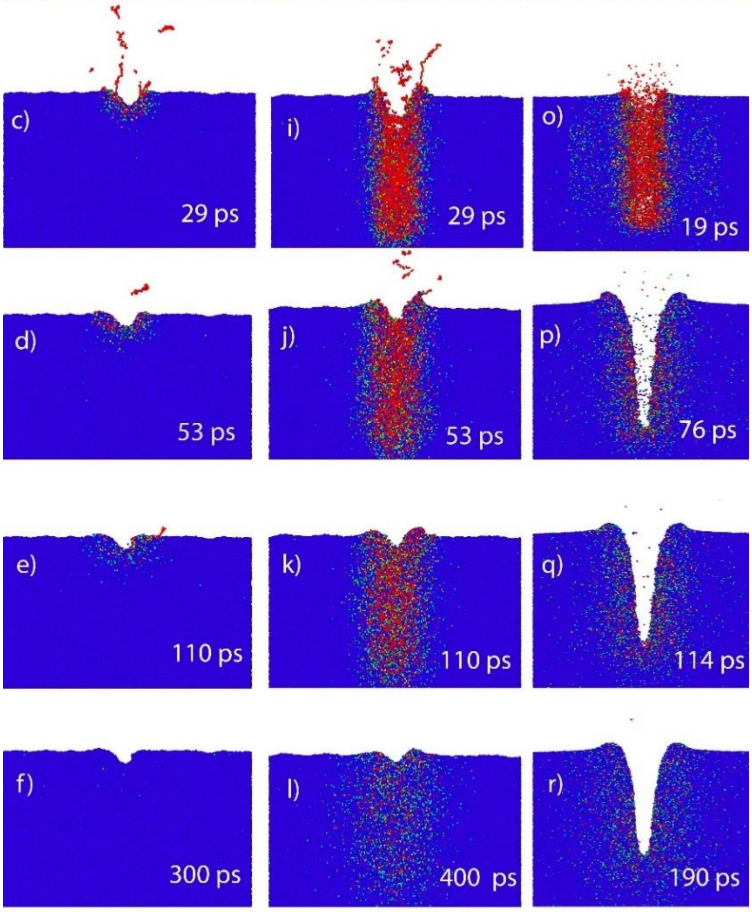

Figure 3. Evolution of a 10 nm FENE film (from a to f), a 60 nm FENE film ( from g to l) and a 60 nm LJ film (from m to r). A color code for kinetic energy was employed, where red depicts particles with kinetic energies higher than the vaporization

temperature and blue particles below melting conditions. For comparison purposes, melting and vaporization temperatures obtained for the LJ system were also kept in the FENE images.

When comparing energy transport in FENE and LJ films of equal thickness, there are qualitative aspects that remain the same: there is a first quick energy dissipation, which can be associated with a pressure pulse, followed by a slower diffusional dissipation during the cooling of the molten region. We computed the displacement of particles from their original positions in the beginning of the simulation and several particles are seen moving coherently. During the simulation, this correlated movement change into a brownian-like movement indicating that after the pressure pulse, energy is transferred as heat. Most particles in deep layers move radially, outwards from the track core. Particles close to the surface have an upward momentum component, while those close to the bottom of the film tend to have a downward movement.

In spite of such similarities, the presence of a chain structure impacts the system evolution, introducing several differences in the final crater shape observed for FENE and LJ thick films. Mobility of particles is severely restricted in the FENE system, where even very hot molecules cannot escape the film. In contrast, hot-particle ejection is very pronounced in the LJ system. Additionally, in the LJ film, melt flow contributes substantially to the transport of mass towards the surface, resulting in a crater hole roughly the size of the entire film thickness and large rims. In FENE samples, however, melt flow acts to repopulate the cavity formed in the early stages of the track evolution, as it can be seen from frame i to j in Fig.3. That is, the hot large molecules in the deep layers move a little upwards, before the systems cool sufficiently to freeze molecular motion. Thus, while melt flow diminishes the final crater depth in the FENE system, in the LJ films it acts as an important mechanism to enlarge the cavity size.

Fig.4 shows top views and lateral slices of the final crater morphology in the end of a simulation of irradiated 20 nm-thick LJ and FENE films. FENE samples present much smaller and less uniform craters when compared with LJ samples (both, the diameter and the depth of the crater are smaller). Crater rims are also small in FENE samples, being slightly larger than the initial roughness of the films, while for the LJ films rims are very pronounced.

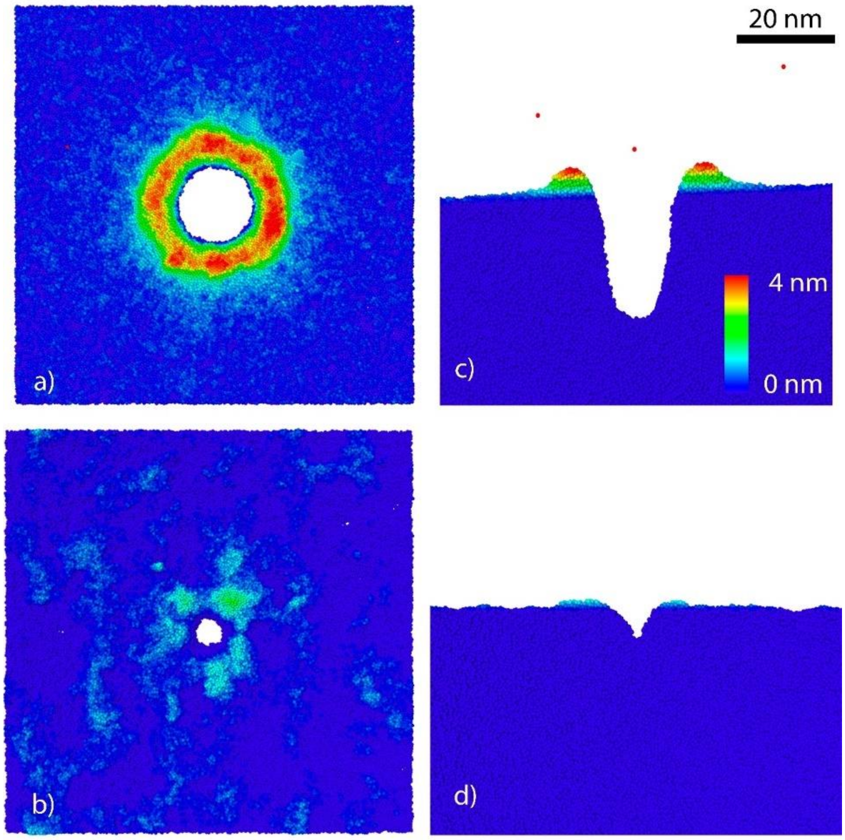

Figure 4. Top and side view of Lennard Jones (a and c) and FENE (b and d) films respectively after system evolution. It was used a collor code for surface height from 0 nm (surface) to 4 nm. It is possible to see that FENE produces smaller and less regular topological effects.

Particle ejection is also influenced by the presence of long chains. In the LJ sample, particles are ejected as isolated particles or small clusters and in the FENE system only entire molecules can be ejected because bond-breaking is artificially blocked. The decreased molecular mobility in FENE samples results in sputtering yields much lower as compared to LJ samples. For a 60 nm thick film, the yield is ~1400 particles/ion (monomers) in the LJ system, reducing to ~800 monomers/ion for the FENE solid. In addition, changes in the chain conformation are clearly seen during the sputtering process in FENE solids. Many molecules that were in a coiled conformation in the beginning of the simulation adopt an extended conformation during ejection, and return to a compact shape after escaping from the solid and cooling down. Thus, part of the excitation energy of the molecules is transferred to internal vibrational modes during the ejection process, what in a real system could lead to in-flight fragmentation. Similar changes in conformation during ejection were also seen in simulations of keV ions bombarding polymeric molecular solids [36,37].

We also evaluated the effect of film thickness in the crater size and sputtering yield. Fig. 5 shows top view AFM-like images of single ion impacts on films of different thicknesses, where the main qualitative differences can be appreciated. The trend found for the FENE films is similar to what has been recently observed for LJ films [31], with craters becoming strongly thickness-dependent below a certain critical thickness, that is different for craters and rims. Rim formation is much more sensitive to the reduction in the thickness of the film than the crater hole. Note that the ion impacts generate craters in LJ films for all thicknesses tested, but for the FENE films at h = 2 nm no crater is formed. This occurs when the track length is similar to the mean gyration radius $R_g$. For very short tracks, only a fraction of the particles in the chain is excited. Even for thicker films, many excited molecules in the simulation that start to escape the solid, recoil back to the surface, most probably because of interchain entragnlement. As $R_g$. grows with chain length, the simulations indicates that the minimum thickness for crater formation (and intact molecular ejection) will increase with molar mass of the polymer.

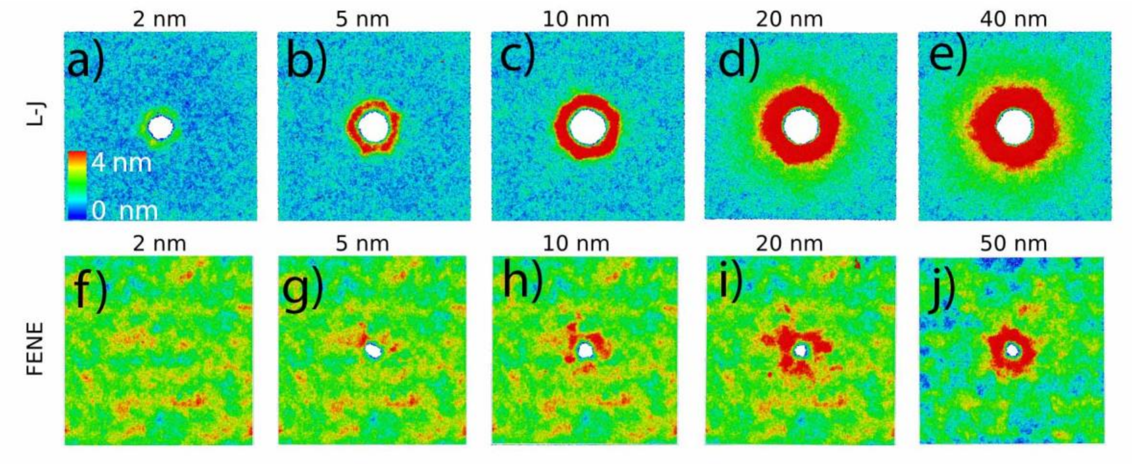

Figure 5. AFM-like images of LJ (a-e) and FENE (f-j) for different film thicknesses (from 2 nm to 50nm). It was used a collor code for surface height from 0 nm (surface) to 4 nm.

The mean crater depth ($Z_{crater}$), crater diameter ($D_{crater}$) and rim volume are displayed as a function of the film thickness in Fig. 6, allowing a more detailed comparison between FENE and LJ results. In the FENE films, $Z_{crater}$ grows quickly with $h$ after the threshold at $h$~2 nm, and already at $h$ ~ 10 nm reaches its maximum value. Beyond that, there is a slight decrease in crater depth until at $h$ ~ 30 nm a plateau region representing the bulk behavior is achieved. This plateau is clearly seen in the experimental data for $h$ > 10 nm. Thus, for FENE system the deepest craters are not found at the thickest films. This is related to the restricted mobility of the chains as already pointed out in the previous section and to the balance of molecules moving into and out the forming crater, which is dependent on the length of the excited track. This is clearly illustrated in Fig. 7, which shows vectors of particle displacement from original positions for 5 nm and 35 nm thick films. In the thin film, while highly excited molecules in the track core leave the material, there is almost no melt flowing into the crater, because the heated track is very short. On the other hand, for the 35 nm film there is a large number of heated particles from the deep regions of the excited track that cannot escape the film, but move into the cavity. Such effect is not seen in the LJ films, because the melt, being very mobile for longer times, contributes to increase crater depth at all tested thicknesses. Differently from the FENE, in the LJ films $Z_{crater}$ increases steadily with $h$ in the entire range of investigated thicknesses. Even at $h$ = 60 nm, $Z_{crater}$ is far from reaching a plateau. Thus, in the thick films, while easy flow of the melt allows large displacement of particles and enlarge craters in LJ systems, the reduced mobility of the “viscous” melt in the FENE film acts for reducing crater depth. This result has not been systematically observed in experiments, although in certain cases craters in thick films appear shallower, although this may be related to the presence of large rims that influence AFM tip penetration into the cavity [31].

$D_{crater}$ also has a region at small $h$ where it is strongly thickness dependent followed by a plateau region where further increase in the track length no longer produces changes (Fig. 6b). In this respect, FENE and LJ films show a similar behavior, although craters are much narrower in the FENE system and reach the plateau level with thinner films (~10 nm) compared to the LJ films (~20 nm). Experiments indicate a critical thickness of ~10 nm below which crater diameter drops quickly [31].

The volume of the crater rim as function of film thickness is displayed in Fig. 6c. Again, FENE rims are smaller when compared to the LJ films for all thickness. For very thin films, the rim in the FENE system is very close to natural roughness of the surface. For both FENE and LJ samples the rim volume grows with increasing thickness until a plateau value is reached. The plateau is reached at similar film thickness: about 35 nm for FENE solids and 30 nm for the LJ case.

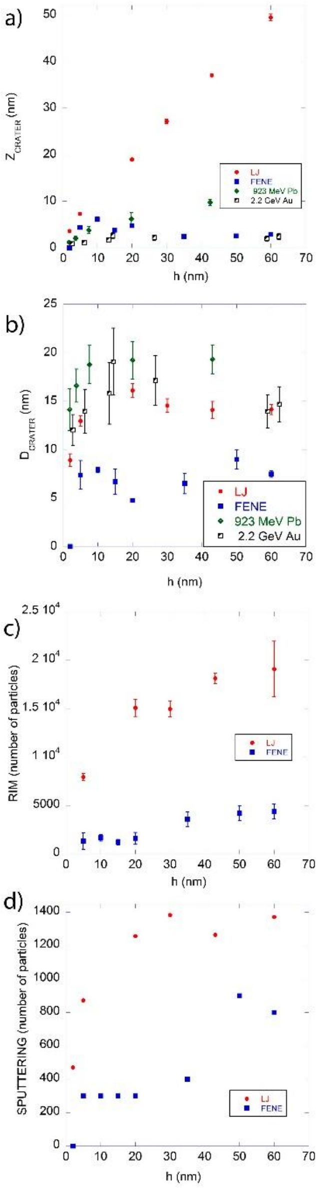

Figure 6. Crater depth (a), Crater diameter (b), rim volume (c), sputtering yield (d) for FENE samples as function of film thickness (from 2 nm to 60 nm). Data for LJ simulations obtained in [31] and for experiments on PMMA films irradiated with 2.2 GeV Au and 923 MeV Pb are also shown. In the FENE simulations, measured crater

diameters fluctuate more in part due to the irregularity of the disposition of the molecules in the sample.

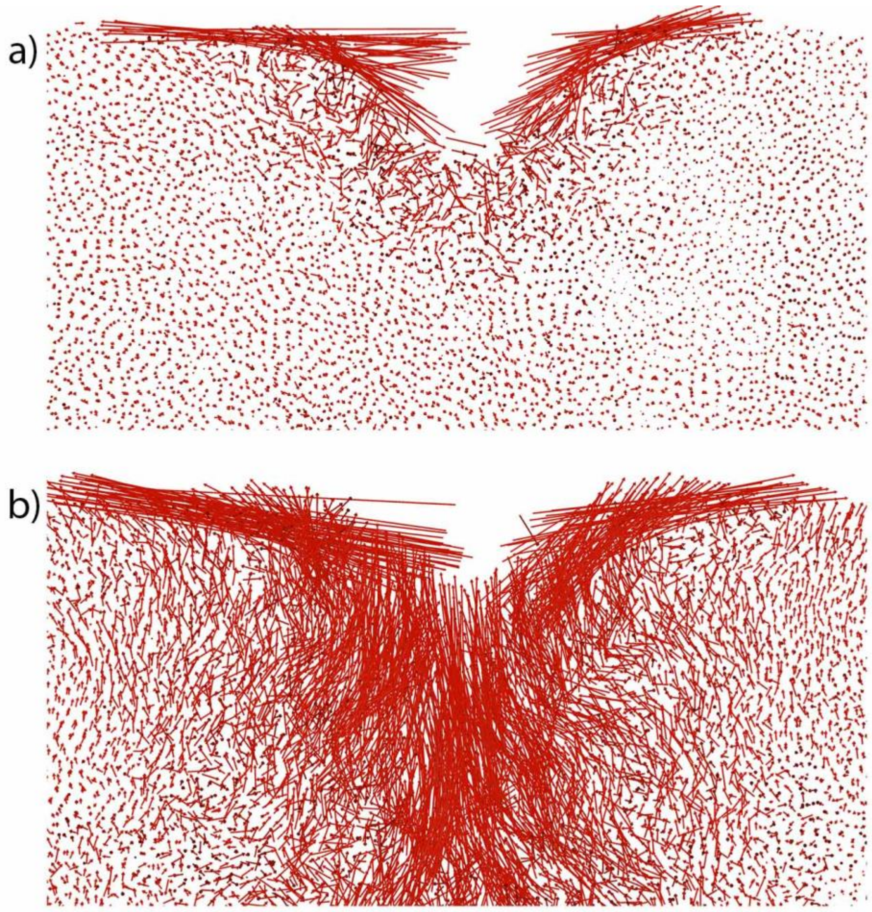

Figure 7. a) Displacement vectors for a 10 nm FENE sample. b) Displacement vectors for a 20 nm FENE sample. The displacement vectors show the displacement of particles from the beginning to the end of the simulation. While in the 10 nm film, all particles move outwards the crater, in the 20 nm, particles from the melt region move towards the crater fulfilling it.The sputtering yield ($Y$) also decreases below certain film thickness (Fig. 6d). This is a result already seen in the early simulation work of Fenyö et al. [28].

Yields are expected to increase until the thickness of the film reaches values equivalent to the maximum depth of origin of sputtered particles in the bulk material ($Z_Y^\infty$). Beyond that $h$, $Y$ grows slowly upon further increase in $h$, until saturation is reached. The computed values of the maximum depth of origin of sputtered particles as a function of $h$ are given in Fig. 8 (we use as criterion to obtain $Z_Y^h$ the maximum depth for which 95% of the particles are emitted). For the LJ molecular solid the saturation yield is reached at about $h$=30 nm and $Z_Y^\infty$~ 22 nm (Fig. 8). In the FENE films, only intact molecules are ejected and because of that the yield growths in steps of 100 particles (1 molecule). The Y saturation thickness is larger for the FENE films and it appears to be around $h$=50 nm, but $Z_Y^\infty$~8 nm. This is surprising, considering that crater volume reaches saturation already at $h$~30 nm and the maximum $Z_{\text{crater}}$ ~3 nm. Thus, FENE simulations show sputtered particles coming from *below* the final crater depth, contrary to what is seen in the LJ film where sputtered particles come always from depths above $Z_{\text{crater}}$ (Fig. 8). This is also in contrast to simulation for keV ions, where the depth of origin of sputtering was found to be not greater than half of the crater depth [37]. Thus in the FENE films, displacement of molecules from deep layers contributes to the sputtering $Y$ *and* to diminish the final crater volume.

We finally note that for very thin films the depth of origin of sputtered particles never reach the entire film thickness. In the FENE samples the depth of origin and the crater depth are always smaller than $h$/2. Similar trends were seen in the experiments with polymer films [31].

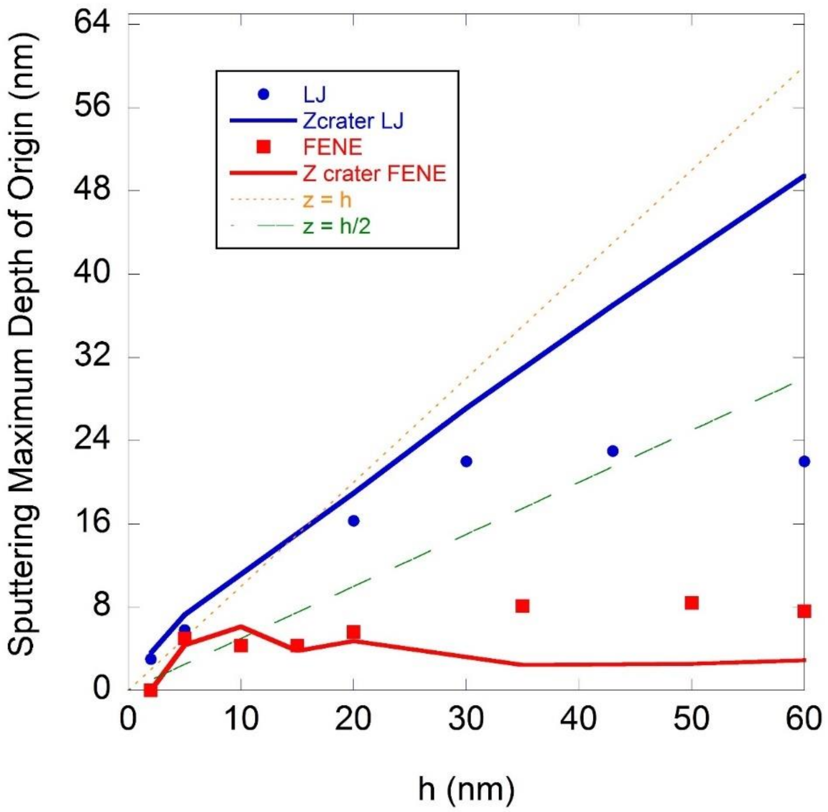

Figure 8. Maximum sputtering depth of origin as function of film thickness for FENE and LJ samples. For comparing purposes, I was added the curves of crater depth (for both potentials) z=h and z=h/2.

## 4. Conclusions

We presented simulations of surface effects produced by a thermal spike on polymer-like films due to the impact of a fast heavy ion, using a coarse-grained approach with the FENE potential. The evolution of the excited track, sputtering and the final surface topology at the impact site were followed as a function of film thickness, and compared to results obtained previously with simulations using LJ potential and experimental data with polymer thin films.

Crater size and sputtering yield are reduced in the FENE systems, compared to LJ films for all thicknesses tested. This is attributed to the additional restrictions to mass transport out of the excited track region imposed by interchain interactions (entanglements) and by the low mobility of the molten phase induced by the spike. Even though crater features in FENE solids are smaller than what is seen experimentally, FENE simulations better match the morphology of the craters seen in polymers and their dependence on film thickness than LJ potentials. However, having the bond-breaking channel inactive, the FENE construct overestimates the system resistance to the ion impact. Since in the inner part of an ion track in a real polymer fragmentation of the chain is extreme, further work is now being conducted aiming more complex potentials capable of dealing with bond breaking and chemical reactions. This will also allow simulating the mass spectra of intact molecules and different fragments to compare to experiments of MeV-SIMS of large organic molecules.

# References

[1] R. Helborg, H. Whitlow, and Y. Zhang, *Ion Beam in Nanoscience and Technology*. Berlin: Srpinger-Verlach, 2009.

[2] R. L. Fleischer, P. Price, and R. M. Walker, *Nuclear Tracks in Solids*. Berkeley: University of California Press, 1975.

[3] J. R. Tesmer and M. Nastasi, *Handbook of Modern Ion Beam Material Analysis*. Pittsburgh: Material Research Society, 1995.

[4] T. Kanai, M. Endo, S. Minohara, N. Miyahara, H. Koyama-Ito, H. Tomura, N. Matsufuji, Y. Futami, A. Fukumura, T. Hiraoka, Y. Furusawa, K. Ando, M. Suzuki, F. Soga, and K. Kawachi, **Int. J. Radiat. Oncol. Biol. Phys., 44, 201 (1999).**

[5] A. Meftah, F. Brisard, J. M. Costantini, E. Dooryhee, M. Hage-Ali, M. Hervieu, J. P. Stoquert, F. Studer, and M. Toulemonde, ***Phys. Rev. B*****, 49, 12457 (1994).**

[6] R. M. Papaleo, *Surface tracks in polymers* in *Fundamentals of Ion-Irradiated Polymers.*, 1ed, D. Fink, Ed. Brlin: Springer-Verlag, 2004.

[7] C. T. Reimann, J. Kopniczky, E. Wistus, J. Eriksson, P. Håkansson, and B. U. R. Sundqvist, ***Int. J. Mass Spectrom. Ion Process.*****, 151, 147 (1995).**

[8] R. . Papaléo, L. . Farenzena, M. . de Araújo, R. . Livi, M. Alurralde, and G. Bermudez, **Nucl. Instruments Methods Phys. Res. Sect. B Beam Interact. with Mater. Atoms, 148, 126 (1999).**

[9] R. Neumann, ***Nucl. Instruments Methods Phys. Res. Sect. B Beam Interact. with Mater. Atoms*****, 151, 42 (1999).**

[10] C. Jeynes, R. P. Webb, and A. Lohstroh, **Reviews of Accelerator Science and Technology. 4, 41 (2011).**

[11] Y. Nakata, Y. Honda, S. Ninomiya, T. Seki, T. Aoki, and J. Matsuo, “Yield enhancement of molecular ions with MeV ion-induced electronic excitation,” ***Appl. Surf. Sci.*****, 255, 1591 (2008).**

[12] J. D. Watrous, P. C. Dorrestein, and J. Wiley, **J. Mass Spectom. 46, 209 ( 2011).**

[13] L. A. Mcdonnell and R. M. A. Heeren, “**Mass Spectrom. Rev. 26, 606 (2007).**

[14] B. U. R. Sundqvist and R. D. Macfarlane, **Mass Spectrom. Rev., 78, 357 (1985).**

[15] W. Ens, B. U. R. Sundqvist, P. Per Harikansson, A. Hedin, and G. Jonsson, ***Phys. Rev. B*****, 39, 763 (1989).**

[16] M. Toulemonde, W. Assmann, C. Trautmann, and F. Grüner, ***Phys. Rev. Lett.*****, 88, 057602 (2002)**

[17] O. Osmani, N. Medvedev, M. Schleberger, and B. Rethfeld, ***Phys. Rev. B*****. 84, 105 (2011).**

[18] H. M. Urbassek, ***Nucl. Instruments Methods B*. 122, 427 (1997)**.

[19] E. Bringa, R. Johnson, and M. Jakas, ***Phys. Rev. B*, 60, 15107 (1999).**

[20] E. M. Bringa and R. E. Johnson, **Nucl. Instruments Methods Phys. Res. Sect. B Beam Interact. with Mater. Atoms, 193, 365(2002).**

[21] E. M. Bringa, R. E. Johnson, and R. M. Papaleo, **Phys. Rev. B, 65, 41131 (2002).**

[22] K. Nordlund and F. Djurabekova, **J. Comput. Electron. 13, 122 (2014).**

[23] R. Smith, M. Harrison, and R. Webb, **Thin Solid Films, 343, 602 (1999).**

[24] J. D. Mody and R. P. Webb, **Surf. Interface Anal., 43, 92 (2011).**

[25] K. Nordlund, J. Peltola, J. Nord, J. Keinonen, and R. S. Averback, ***J. Appl. Phys.*, 90, 1710 (2001).**

[26] E. M. Bringa and R. E. Johnson, ***Nucl. Instruments Methods Phys. Res. Sect. B Beam Interact. with Mater. Atoms*, 143, 513 (1998).**

[27] H. M. Urbassek, H. Kafemann, and R. E. Johnson, ***Phys. Rev. B*, 49, 786 (1994).**

[28] R. J. D. Fenyö, R.E. Johnson, ***Phys. Rev. B*, 46, 5090 (1992).**

[29] E. M. Bringa, E. Hall, R. E. Johnson, and R. M. Papaléo, **Nucl. Instruments Methods Phys. Res. Sect. B Beam Interact. with Mater. Atoms, 193, 734 (2002).**

[30] R. M. Papaléo, R. Leal, C. Trautmann, and E. M. Bringa, **Nucl. Instruments Methods Phys. Res. Sect. B Beam Interact. with Mater. Atoms, 206, 7 (2003**).

[31] R. M. Papaléo, R. Thomaz, L. I. Gutierres, V. M. de Menezes, D. Severin, C. Trautmann, D. Tramontina, E. M. Bringa, and P. L. Grande, **Phys. Rev. Lett., 114, 1 (2015).**

[32] K. Kremer and G. S. Grest, “Dynamics of entangled linear polymer melts: A molecular-dynamics simulation,” **J. Chem. Phys., vol. 92, 5057 (1990).**

[33] M. Bulacu and E. Van Der Giessen, **J. Chem. Phys., 123, 11 (2005).**

[34] B. Z. Dlugogorski, M. Grmela, and P. J. Carreau, **Rheol. Acta, vol. 34, 384 (1995**).

[35] B. Z. Dlugogorski, M. Grmela and P. J. Carreau, **J. Non-newtonian Fluid Mech, 49 23 (1993).**

[36] A. Delcorte, O. a. Restrepo, K. Hamraoui, and B. Czerwinski, ***Surf. Interface Anal.*, vol. 46, 46 (2014).**

[37] A. Delcorte, B. J. Garrison, C. D. Lou V, C. Sud, B.-L. V V, T. Pennsyl, V. State, V. Uni, U. V Park, and V. Pennsyl, **J. Phys. Chem. 111, 15312 (2007)**

[38] S. Plimpton, ***J. Comput. Phys.*, 117, 1 (1995).**

[39] E. Bringa, R. Johnson, and R. Papaléo, ***Phys. Rev. B*, vol. 65, no. 9, pp. 1–8(2002).**

[40] G. Szenes, K. Havancsák, V. Skuratov, P. Hanák, L. Zsoldos, and T. Ungár, ***Nucl. Instruments Methods Phys. Res. Sect. B Beam Interact. with Mater. Atoms*, 166, 933 (2000).**

[41] A. Stukowski, **Model. Simul. Mater. Sci. Eng., 18, 015012 (2009).**

# 5. CONSIDERAÇÕES FINAIS

Nesse trabalho, os efeitos da radiação iônica de alta energia (no regime de freamento eletrônico) em filmes finos orgânicos foram investigados usando Simulação Computacional por Dinâmica Molecular. Utilizou-se um modelo de Thermal Spike para modelar a deposição de energia pelo íon no material e dois potenciais de interação na escala granular foram aplicados para descrever o material: o potencial de Lennard-Jones (em que não se permite a existência de cadeias moleculares) e o potencial FENE (em que se permite a construção de cadeias moleculares). A partir disso, dois trabalhos foram submetidos para publicação.

O primeiro trabalho, apenas com os resultados dos sólidos de Lennard-Jones, está associado ao trabalho de mestrado de Leandro Gutierres, e do qual participei ativamente ao longo deste projeto. Nesse artigo, mostrou-se a dependência dos efeitos da radiação no sólido de Lennard-Jones em relação à espessura do filme irradiado e em relação ao poder de fretamento do íon incidente. As principais conclusões desse trabalho indicam que as dimensões da cratera tornam-se sensíveis à espessura do filme abaixo de 10 nm enquanto que o volume da protuberância torna-se sensível abaixo de 30 nm.

O segundo trabalho apresenta uma comparação dos resultados obtidos com o sólido FENE e com o sólido Lennard-Jones, tendo sido o tema principal dessa pesquisa. O artigo submetido para publicação será o primeiro trabalho a apresentar simulações de Thermal spike em um sólido modelado pelo potencial FENE na faixa de energia do freamento eletrônico.

Utilizar o potencial FENE trouxe um maior realismo às simulações, comparando-se com o primeiro artigo, pois permitiu a introdução de cadeias moleculares no sólido irradiado. Essa única alteração mudou significativamente os resultados obtidos, aproximando-os dos dados experimentais e trazendo novos *insights* sobre o tema de estudo. Além da redução de todos os efeitos da radiação, a presença de cadeias moleculares trouxe três resultados inéditos.

O primeiro resultado inédito foi encontrar uma espessura limiar para o aparecimento de efeitos da radiação, sendo esse limiar aproximadamente igual ao raio de giração médio das moléculas da amostra, indicando que moléculas parcialmente excitadas podem não ter energia suficiente para serem ejetadas do material.

O segundo resultado inédito foi encontrar as maiores dimensões da cratera em filmes menos espessos do que o *bulk,* o que difere dos resultados da literatura.

Isso foi, então, explicado pelo papel desempenhado pela região derretida (*melt region*), que escorre e preenche a cratera em filmes mais espessos, o que pode ser considerado nosso terceiro resultado inédito.

Em trabalhos futuros, deve-se buscar o avanço em direção a simulações mais realistas, que permitam, por exemplo, a quebra de ligação e a construção de amostras com cadeias de diferentes tamanhos, no nível granular. Além disso, deve-se buscar a implementação de potenciais mais complexos, no nível atomístico, como ReaxFF, que permita o estudo de danos químicos.

# 6. REFERÊNCIAS BIBLIOGRÁFICAS

[1] A. M. Allen, T. Pawlicki, L. Dong, E. Fourkal, M. Buyyounouski, K. Cengel, J. Plastaras, M. K. Bucci, T. I. Yock, L. Bonilla, R. Price, E. E. Harris, and A. a. Konski, “An evidence based review of proton beam therapy: The report of ASTRO’s emerging technology committee,” *Radiother. Oncol.*, vol. 103, no. 1, pp. 8–11, 2012.

[2] T. Kanai, M. Endo, S. Minohara, N. Miyahara, H. Koyama-Ito, H. Tomura, N. Matsufuji, Y. Futami, A. Fukumura, T. Hiraoka, Y. Furusawa, K. Ando, M. Suzuki, F. Soga, and K. Kawachi, “Biophysical characteristics of HIMAC clinical irradiation system for heavy-ion radiation therapy,” *Int. J. Radiat. Oncol. Biol. Phys.*, vol. 44, no. 1, pp. 201–210, 1999.

[3] H. Ryu, E. Song, J. Lee, and J. Kim, “Density and spatial resolutions of proton radiography using a range modulation technique.,” *Phys. Med. Biol.*, vol. 53, no. 19, pp. 5461–5468, 2008.

[4] M. Bucciantonio and F. Sauli, “Proton computed tomography,” *Mod. Phys. Lett. A*, vol. 30, no. 17, p. 1540024, 2015.

[5] K. Iniewski, *Radiation Effects in Semiconductors (Devices, Circuits, and Systems)*. CRC Press, 2010.

[6] Paul van der Heide, *Secondary Ion Mass Spectrometry: An Introduction to Principles and Practices*. Wiley, 2014.

[7] C. Jeynes, R. P. Webb, and A. Lohstroh, “Ion Beam Analysis: A Century of Exploiting the Electronic and Nuclear Structure of the Atom for Materials Characterisation,” *Rev. Accel. Sci. Technol.*, vol. 04, no. 01, pp. 41–82, 2011.

[8] Y. Nakata, Y. Honda, S. Ninomiya, T. Seki, T. Aoki, and J. Matsuo, “Yield enhancement of molecular ions with MeV ion-induced electronic excitation,” *Appl. Surf. Sci.*, vol. 255, no. 4, pp. 1591–1594, 2008.

[9] L. A. McDonnel and R. M. A. Heeren, “Imagin Mass Spectrometry,” *Mass Spectrom. Rev.*, vol. 26, pp. 606–643, 2007.

[10] J. D. Watrous, T. Alexandrov, and P. C. Dorrestein, “The evolving field of imaging mass spectrometry and its impact on future biological research,” *J. Mass Spectrom.*, vol. 46, no. 2, pp. 209–222, 2011.

[11] M. J. Bailey, B. N. Jones, S. Hinder, J. Watts, S. Bleay, and R. P. Webb, “Depth profiling of fingerprint and ink signals by SIMS and MeV SIMS,” *Nucl. Instruments Methods Phys. Res. Sect. B Beam Interact. with Mater. Atoms*, vol. 268, no. 11–12, pp. 1929–1932, 2010.

[12] P. Apel, a Schulz, R. Spohr, C. Trautmann, and V. Vutsadakis, “Track size and track structure in polymer irradiated by heavy ions,” *Nucl. Instruments Methods Phys. Res. Sect. B Beam Interact. with Mater. Atoms*, vol. 146, no. 1–4, pp. 468–474, 1998.

[13] R. Hellborg, H. J. Whitlow, and Y. Zhang, “Ion Beams in Nanoscience and Technology,” *Configurations*, pp. 107–127, 2010.

[14] R. Spohr, “Status of ion track technology - Prospects of single tracks,” *Radiat. Meas.*, vol. 40, no. 2–6, pp. 191–202, 2005.

[15] J. Dutta, G. L. . Hornyak, J. J. . Moore, and H. . Tibbals, *Fundamentals of Nanotechnology*. CRC Press, 2008.

[16] M. M. Jakas, “Fluid dynamics calculation of sputtering,” *Nucl. Instruments Methods Phys. Res. Sect. B Beam Interact. with Mater. Atoms*, vol. 193, no. 1–4, pp. 727–733, 2002.

[17] K. Nordlund and F. Djurabekova, “Multiscale modelling of irradiation in nanostructures,” *J. Comput. Electron.*, vol. 13, no. 1, pp. 122–141, 2014.

[18] D. C. Rapaport, *Art of Molecular Dynamics*, 2nd ed. New York: Cambridge University Press, 2004.

[19] “Laboratório de Alto Desempenho - LAD-PUCRS.” [Online]. Available: http://www3.pucrs.br/portal/page/portal/ideia/Capa/LAD.

[20] S. Plimpton, “Fast Parallel Algorithms for Short – Range Molecular Dynamics,” *J. Comput. Phys.*, vol. 117, no. June 1994, pp. 1–19, 1995.

[21] R. E. Johnson, “Thermal Spike and Sputtering Yields,” *Radiat. Eff.*, vol. 52, pp. 187–190, 1980.

[22] E. M. Bringa and R. E. Johnson, “Molecular dynamics study of non-equilibrium energy transport from a cylindrical track,” *Nucl. Instruments Methods Phys. Res. Sect. B Beam Interact. with Mater. Atoms*, vol. 143, no. 4, pp. 513–535, 1998.

[23] E. Bringa, R. Johnson, and M. Jakas, “Molecular-dynamics simulations of electronic sputtering,” *Phys. Rev. B*, vol. 60, no. 22, pp. 15107–15116, 1999.

[24] B. Dünweg and K. Kremer, “Molecular dynamics simulation of a polymer chain in solution,” *J. Chem. Phys.*, vol. 99, no. 9, p. 6983, 1993.

[25] R. Spohr, *Ion tracks and microtechnology - Principles and Applications*. ViewegTeubner Verlag, 1990.

[26] R. L. . FLEISCHER, P. B. . PRICE, and R. M. WALKER, *Nuclear Tracks in Solids: Principles and Applications*. University of California Press, 1975.

[27] NIST, “PSTAR,” 2016. [Online]. Available: http://physics.nist.gov/PhysRefData/Star/Text/PSTAR.html. [Accessed: 07-Nov-2016].

[28] R. M. Papaleo, “Fas ion induced sputtering and Modification of Molecular Solids,” Acta Universitatis Upsaliensis, 1996.

[29] G. Szenes, K. Havancsák, V. Skuratov, P. Hanák, L. Zsoldos, and T. Ungár, “Application of the thermal spike model to latent tracks induced in polymers,” *Nucl. Instruments Methods Phys. Res. Sect. B Beam Interact. with Mater. Atoms*, vol. 166, pp. 933–937, 2000.

[30] E. M. Bringa and R. E. Johnson, “Electronic sputtering of solid O2,” *Surf. Sci.*, vol. 451, no. 1, pp. 108–115, 2000.

[31] R. . Papaléo, L. . Farenzena, M. . de Araújo, R. . Livi, M. Alurralde, and G. Bermudez, “Cratering in PMMA induced by gold ions: dependence on the projectile velocity,” *Nucl. Instruments Methods Phys. Res. Sect. B Beam Interact. with Mater. Atoms*, vol. 148, no. 1–4, pp. 126–131, 1999.

[32] R. M. Papaléo, R. Leal, C. Trautmann, and E. M. Bringa, “Cratering by MeV-GeV ions as a function of angle of incidence,” *Nucl. Instruments Methods Phys. Res. Sect. B Beam Interact. with Mater. Atoms*, vol. 206, pp. 7–12, 2003.

[33] E. Bringa, R. Johnson, and R. Papaléo, “Crater formation by single ions in the electronic stopping regime: Comparison of molecular dynamics simulations with experiments on organic films,” *Phys. Rev. B*, vol. 65, no. 9, pp. 1–8, 2002.

[34] R. E. Johnson and J. Schou, “Sputtering of inorganic insulators,” *Fundamental processes in sputtering of atoms and molecules*. p. 403, 1993.

[35] E. M. Bringa, M. Jakas, and R. E. Johnson, “Spike models for sputtering: Effect of the surface and the material stiffness,” *Nucl. Instruments Methods Phys. Res. Sect. B Beam Interact. with Mater. Atoms*, vol. 164, pp. 762–771, 2000.

[36] R. M. Papaléo, R. Thomaz, L. I. Gutierres, V. M. de Menezes, D. Severin, C. Trautmann, D. Tramontina, E. M. Bringa, and P. L. Grande, “Confinement Effects of Ion Tracks in Ultrathin Polymer Films,” *Phys. Rev. Lett.*, vol. 114, no. 11, pp. 1–5, 2015.

[37] E. M. Bringa, E. Hall, R. E. Johnson, and R. M. Papaléo, “Crater formation by ion bombardment as a function of incident angle,” *Nucl. Instruments Methods Phys. Res. Sect. B Beam Interact. with Mater. Atoms*, vol. 193, no. 1–4, pp. 734–738, 2002.

[38] R. M. Papaléo, “Surface tracks on polymers: A means to probe material properties at the nanometer scale?,” *Nucl. Instruments Methods Phys. Res. Sect. B Beam Interact. with Mater. Atoms*, vol. 191, no. 1–4, pp. 669–674, 2002.

[39] R. M. Papaléo, M. R. Silva, R. Leal, P. L. Grande, M. Roth, B. Schattat, and G. Schiwietz, “Direct evidence for projectile charge-state dependent crater formation due to fast ions,” *Phys. Rev. Lett.*, vol. 101, no. 16, pp. 1–4, 2008.

[40] R. . J. D. Fenyö, “Computer experiments on molecular ejection from an amorphous solid: Comparison to a analytic continuum mechanical model,” *Phys. Rev. B*, vol. 46, no. 9, pp. 5090–5099, 1992.

[41] R. S. Thomaz, “Efeitos da Radiação Iônica em Polímeros sob Confinamento Espacial em Uma Dimensão,” Pontifícia Universidade Católica do Rio Grande do Sul, 2015.

[42] E. M. Bringa, R. E. Johnson, and R. M. Papaleo, “Crater formation by fast ions: comparison of experiment with Molecular Dynamics simulations,” p. 7, 2001.

[43] T. Wu, “Advantages of a Finite Extensible Nonlinear Elastic Potential in Lattice Boltzmann Simulations,” vol. 7, no. 1, 2014.